Actomyosin Contractility is a Potent Suppressor of Mesoderm Induction by Human Pluripotent Stem Cells

Loic Fort[1,3], Vaishna Vamadevan[1], Wenjun Wang[2], and Ian G. Macara[1,3]

[1] Dept of Cell and Developmental Biology, Vanderbilt University School of Medicine, Nashville TN 37240 USA

[2] Dept of Biomedical Engineering, Vanderbilt University Nashville TN 37240 USA

[3] Authors for correspondence

Abstract

The activation of WNT signaling in human pluripotent stem cells (hPSCs) drives efficient conversion to lateral mesoderm, which can be further differentiated into cardiomyocytes. Stabilization of the WNT effector β-catenin promotes expression of mesoderm-specifying genes such as *TBXT* (which encodes Brachyury) and drives an epithelial-mesenchymal transition (EMT). Mechanical forces are essential for the self-organization and development of vertebrate embryos but the role of forces, especially actomyosin contractility, in mesoderm specification has remained controversial. We discovered that, unexpectedly, increasing actomyosin contractility by expression of constitutively active Rho kinase or MLC kinase, efficiently blocked any induction of mesoderm by WNT signaling, and cells failed to undergo EMT. Conversely, the suppression of contractility by inhibitors and genetic approaches significantly accelerated differentiation: Brachyury induction was enhanced, and EMT initiated 24hrs earlier than in control settings. These data were initially puzzling because we observed that WNT signaling was sufficient by itself to promote contractility of hiPSC colonies. Notably, however, we showed that contractility must be inhibited prior to WNT activation to efficiently promote mesoderm specification, suggesting that reduced tension primes the pluripotent state, not the induced state, to accelerate differentiation along this trajectory. Mechanistically, we found that loss of contractility decreased junctional β-catenin and promoted active β-catenin levels in the cytoplasm and nucleus. Increased contractility had opposite effects, highlighting actomyosin contractility at the pluripotent state as a key regulator of WNT signaling responsiveness through effects on adherens junctions.

Introduction

Mechanical forces play major roles at many stages of animal development: Starting as early as compaction at the 8-cell stage [1], mechanics plays a central role in self-organization to shape the embryo [2–5]. In vitro, the differentiation of pluripotent stem cells (PSCs) into germ layers is governed by dynamic interplay between mechanical forces, signaling cues, and transcriptional regulators. Internal forces are largely generated by actomyosin contractility, and in epithelia are transmitted across cell boundaries by intercellular junctions, enabling collective organization [6–11]. But how actomyosin contractility is coupled to cell fate specification through target gene expression has remained unclear.

Human embryonic stem cell (hESC) and induced pluripotent stem cell (hiPSC) colonies can be induced to select the mesoderm lineage and eventually to differentiate into functional cardiomyocytes [12–14] Both types of PSCs are strongly epithelial, and lineage specification relies on an epithelial-to-mesenchymal transition (EMT) that is reminiscent of some aspects of gastrulation [15–17] .

Mesoderm can also be generated from hPSCs by direct WNT pathway activation using the small molecule GSK3β inhibitor Chiron 99021 (hereafter CHIR), which protects cytosolic β-catenin from degradation through a similar mechanism to WNT ligand signaling. The stabilized β-catenin then enters the nucleus and binds to TCF transcription factors at target gene promoters. A separate pool of β-catenin in epithelial cells is tightly associated with E-cadherin at the adherens junctions, but whether this pool contributes to WNT signaling and mesoderm induction by hPSCs, or participates in WNT responses in other situations, remains controversial [18]. For example, increased junctional β-catenin has been reported to correlate with increased nuclear β-catenin, though the mechanism for this phenomenon was not explained [17]. To the contrary, in *Drosophila* imaginal disks, actomyosin contractility can promote E-cadherin accumulation at adherens junctions[11], which reduces β-catenin-mediated gene expression [11], while deletion of E-cadherin promotes WNT-responsive gene expression [19]. These studies in *Drosophila* suggest that cytoplasmic β-catenin and β-catenin at the adherens junctions are dynamically linked, but whether a similar titration system applies in human cells and, particularly in hPSCs, remains unknown. Although there are multiple studies on the impact of extracellular matrix stiffness [16,17], tissue confinement [20], and EMT [21] on the E-cadherin/β-catenin

interaction and its downstream consequences, there has been to our knowledge no direct interrogation of how actomyosin contractility impacts mesoderm commitment by hPSCs.

From prior work on BMP4-driven mesoderm in hESCs [16,17], we expected that inhibiting actomyosin activity would block induction. Surprisingly, however, we obtained the opposite result: increasing contractility was sufficient to completely block differentiation and EMT, while suppressing MLC phosphorylation using small molecule inhibitors or genetic tools substantially promoted mesoderm induction. These data were also puzzling because induction of differentiation alone promotes contractility of stem cell colonies. However, we discovered that the effects of elevated or suppressed actomyosin contractility have a temporal dependence, since their effects on differentiation depend on priming of the pluripotent state, not on events post-induction. Mechanistically, we found that promoting cell relaxation led to loss of β-catenin from cell junctions and an increase in active β-catenin in the cytoplasm and nucleus, suggesting that the β-catenin pools are dynamically coupled through actomyosin contractility to control mesoderm specification.

Results

Contractility is a potent inhibitor of mesoderm identity

We initially hypothesized that actomyosin contractility might support mesoderm specification, given prior reports implicating mechanical forces in lineage commitment [5,16,17]. The broad-spectrum phosphatase inhibitor Calyculin A has been used in several studies of the impact of enhanced contractility on embryonic development [5,9] but it blocks dephosphorylation of scores of proteins, not just ppMLC. Therefore, we treated WT hiPSCs before and during differentiation with RhoA activator II (CN03), a highly specific bacterial toxin derivative that converts the RhoA Glutamine 63 to Glutamate, locking RhoA in a constitutively active form [22,23], which will then specifically activate ROCK to phosphorylate MLC (**Supplementary Figure 1A**). Staining for phospho-T18/S19 Myosin Light Chain 2 (ppMLC2) confirmed that CN03 treatment led to higher levels of contractility by 24 hrs post-CHIR addition (**Supplementary Figure 1B**). Strikingly, CN03-treated cells failed to express any detectable Brachyury (encoded by *TBXT* gene, also known as *T* gene), a mesoderm marker. (**Supplementary Figure 1C-D**). However, CN03 treatment caused cell toxicity past 48h, preventing further analysis.

93 For this reason, we turned to genetic approaches by stably expressing constitutively
94 active ROCK2 or MLCK (ROCK2^{CA} and MLCK^{CA}) under a Doxycycline inducible promoter, with
95 constitutive expression of a Venus reporter. We first confirmed that Venus^{Pos} cells treated with
96 Doxycycline showed signs of higher contractility. In co-cultures containing ROCK2^{CA}/WT or
97 MLCK^{CA}/WT cells treated with Doxycycline, Venus^{Pos} clusters showed strong cortical F-actin and
98 higher ppMLC2 staining organized as fibers, compared to WT Venus^{Neg} cells, which show more
99 diffuse staining (**Supplementary Figure 1E, G**). These data support the idea that Venus^{Pos} cells
100 experience higher contractility, allowing us to test the impact on cell fate. As an in situ control
101 unlabeled WT hiPSCs were mixed 1:1 with green (Venus^{Pos}) transduced cells, and the cultures
102 were pre-treated with Doxycycline (or vehicle) to turn on ROCK2^{CA} or MLCK^{CA} before starting the
103 differentiation protocol. We prolonged the differentiation to 72 hrs in this co-culture system to
104 better assess the impact of enhanced contractility (**Figure 1A**). Venus-positive and negative
105 areas were outlined based on Venus expression across clusters (**Supplementary Figure 1F, H**)
106 and percentages of cells expressing mesoderm and EMT markers were measured. Strikingly,
107 following 72h of differentiation in the presence of doxycycline, Venus^{Pos} clusters of ROCK2^{CA}
108 cells showed a dramatic decrease in mesoderm (**Figure 1B, C**), primitive streak (**Figure 1D, E**)
109 compared to Venus^{Neg} cells or Vehicle-treated cells. Venus^{Pos} cells also failed to undergo EMT,
110 which usually occurs 50-52h post differentiation, as observed by the absence of Slug expression
111 and the persistence of epithelial marker ZO-1 (**Figure 1F-H**).
112 In addition to ROCK2, MLC2 phosphorylation was previously shown to be spatially
113 regulated by Myosin Light Chain Kinase (MLCK) in polarized and non-polarized cells [24,25] .
114 Therefore, we also probed the effect of MLCK-driven contractility on cell identity by expressing a
115 constitutively active mutant. Consistent with the effects of ROCK2^{CA}, MLCK^{CA}-positive clusters
116 failed to commit to the primitive streak and mesoderm lineage and to trigger the EMT program
117 required for mesoderm identity (**Supplementary Figure 1I-K**). These data support the surprising
118 conclusion that activation of ROCK/MLCK-mediated contractility is sufficient to counteract the
119 effect of WNT signaling activated by CHIR and completely prevents mesoderm conversion and
120 EMT.
121
122 <u>Genetic suppression of actomyosin contractility promotes stem cell conversion to the</u>
123 <u>mesoderm lineage</u>

124 This unexpected finding prompted us to investigate whether inhibition of contractility might
125 conversely promote mesoderm differentiation. We designed a genetic approach to suppress
126 contractility in human cells. Dephosphorylation of ppMLC is mediated by MLC Phosphatase, a
127 heterotrimer composed of a catalytic subunit PP1cβ, a Myosin phosphatase-targeting regulatory
128 subunit (MYPT1) and a protein of unknown function M20 [26,27] (**Figure 2A-B**). Based on previous
129 work describing an optogenetic construct to control actomyosin contractility [28], we created a
130 truncated MYPT1, fused with a nuclear export sequence and a mNeonGreen (mNG) reporter
131 (**Figure 2B**), which is expected to act as a constitutively active mutant and promote MLC2
132 dephosphorylation.
133 To validate the activity of this new tool, we cloned the construct (referred to as
134 MYPT1^{CA}-NES-mNG) under a doxycycline-inducible promoter and established a stable hiPSC line.
135 Global reduction of ppMLC2 was observed by immunoblot and immunofluorescence after
136 doxycycline addition (**Figure 2C-E**). Strikingly, MYPT1^{CA} cells pre-treated overnight with
137 doxycycline and followed by differentiation (**Figure 2F**), displayed enhanced Brachyury
138 expression (**Fig 2G-K**) and earlier induction of the EMT genes Snail and Slug (**Figure 2G**)
139 following Doxycycline induction, compared to controls. Because apoptosis is crucial to enable
140 mesoderm fate specification [15] we probed for PARP cleavage as an apoptosis marker but did not
141 detect any difference (**Figure 2I**). We conclude that reducing MLC2-driven contractility
142 significantly accelerates mesoderm specification.
143
144 <u>Promotion of hiPSC and hESC conversion to the mesoderm lineage by actomyosin relaxation is</u>
145 <u>time-dependent</u>
146 We next used small molecule inhibitors as an orthogonal method to validate our
147 previous findings. This approach allowed us to expand our investigation to hESCs, while also
148 providing better control over the timing of inhibition.
149 First, hiPSCs were pre-treated overnight with the ROCK inhibitor, Y-27632 to suppress
150 actomyosin contractility at the pluripotent state then differentiated by addition of CHIR in the
151 continued presence Y-27632 (**Figure 3A**). We confirmed that MLC2 phosphorylation was
152 reduced by ROCK inhibition **(Supplementary Figure 2A-B)**. Similar to the genetic approach,
153 pharmaceutical blockage of contractility strongly promoted Brachyury expression **(Figure 3B-C)**.
154 Expression of other key mesoderm (*MESP1* and *TBX6*) and EMT (*SNAI1* and *SNAI2*) genes was

155 also upregulated following Y-27632 treatment **(Figure 3D-G)**. To rule out an effect of ROCK
156 inhibition on global transcription, we examined expression levels of genes unrelated to
157 mesodermal fate and did not detect any response to decreased contractility, suggesting a
158 specific role for actomyosin contractility in mesoderm specification **(Supplementary Figure 2C)**.
159 At the cellular level, Brachyury expression is initially restricted to the colony edges at
160 24hrs, before broader expression across the colony at later timepoints (**Figure 3H-I**). However, Y-
161 27632 treatment resulted in more widespread Brachyury expression **(Figure 1H-I)**, markedly
162 accelerated EMT as shown by loss of the epithelial marker ZO-1 from tight junctions (**Figure 1H,**
163 **J**), and increased expression of the mesenchymal marker Slug **(Supplementary Figure 2D)**. To
164 validate these data, we used a more specific ROCK inhibitor, H-1152, which led to similar
165 decreases in ppMLC2 **(Supplementary Figure 2E-F)** and recapitulated the early EMT and higher
166 induction of mesoderm markers **(Supplementary Figure 2G-M)**. Apoptosis was not affected
167 following Y-27632 or H-1152 treatment **(Supplementary Figure 2L)**. Moreover, these effects of
168 ROCK inhibition were conserved in hESCs expressing a knock-in T-mNeonGreen fusion [16] **(Figure**
169 **3K-L)** and in wild-type H9 hESCs treated with CHIR (**Supplementary Figure 2N-O**). Importantly,
170 similar to hiPSCs, there was no effect of reduced contractility on apoptosis initiation
171 (**Supplementary Figure 2N and 2P**) or on exit from the pluripotency state **(Supplementary**
172 **Figure 2N and 2Q)**.
173 Because MLCK activation was sufficient to block cell commitment (**Supplementary**
174 **Figure 1I-K**), we tested the effect of ML-7, a potent MLCK inhibitor [29]. ML-7 led to efficient
175 reduction in ppMLC2 **(Figure 3M-N)** and strongly enhanced Brachyury expression at 48hrs**,**
176 without affecting cell death **(Figure 3O-P)**. Together these data show, unexpectedly, that
177 pharmacological blockade of MLC2-mediated force generation enhances mesoderm
178 commitment quantitatively and accelerates the EMT required for conversion to cardiac
179 mesoderm.
180 These results were particularly surprising, because hiPSC colonies show rapid retraction
181 of their edges following CHIR addition **(Supplementary Figure 3A and Supplementary Video 1)**,
182 consistent with observations from other groups [30]. Having previously reported an essential and
183 permissive role for apoptosis during mesoderm specification [15], we tested whether colony
184 retraction was related to the wave of cell death that follows CHIR addition. However, co-

185 treatment with a pan-Caspase inhibitor (Q-VD-OPH) did not prevent retraction of colony edges
186 **(Supplementary Figure 3A)**, ruling out an effect of cell density and cell death.
187 Commitment to the mesoderm lineage also resulted in thicker epithelial layers,
188 containing taller cells **(Supplementary Figure 3B-D)**, suggesting morphological changes that are
189 highly dependent on the cellular contractile state. Consistent with the role of nuclei as a
190 mechanosensor [31,32], differentiating cells exhibit significantly smaller nuclear area after 48h of
191 CHIR treatment **(Supplementary Figure 3E-F)**. To address the variation of cell density, we
192 correlated each of our nuclear area measurements with the actual cell number **(Supplementary**
193 **Figure 3G)**. As expected, nuclear area negatively correlates with cell density before
194 differentiation. However, we did not find any correlation following CHIR treatment, together
195 suggesting that the smaller nuclear size at 48h of differentiation is unlikely to be related to cell
196 density.
197 While these observations were indirect, they point towards a change in contractile
198 status during mesoderm commitment. To directly test for higher contractility, differentiating
199 cells were stained ppMLC2. Immunofluorescence revealed a gradual increase of ppMLC2
200 intensity over time **(Supplementary Figure 3H-I)**. Finally, we took advantage of the birefringence
201 property of actin fibers to measure optical retardance using quantitative polarization
202 microscopy [33]. Birefringence of a material changes proportionally to the applied strain,
203 providing an orthogonal way to probe for contractile status during mesoderm commitment.
204 Confirming our previous data, retardance values increased during hiPSC-to-mesoderm
205 conversion **(Supplementary Figure 3J)**. Specificity of the retardance value as a readout for
206 contractility was tested by incubating undifferentiated hiPSCs with Y-27632, which reduced
207 retardance. Together, these data suggest that hiPSC differentiating along the cardiac mesoderm
208 trajectory, in the absence of any external perturbation, experience increasing contractile forces
209 mediated by MLC2 phosphorylation.
210 How can we reconcile the surprising observation that differentiating cells intrinsically
211 become more contractile, with the inhibitory function of actomyosin contractility on
212 mesodermal specification? We wondered if the timing of inhibitor treatment was important,
213 and therefore staggered the timing such that Y-27632 was added either 12 hrs prior
214 differentiation (-12h), at the time of differentiation (0h) or 12 hrs following CHIR treatment
215 (+12h), and analyzed Brachyury expression after 24hrs post-CHIR addition (**Figure 3Q**). Pre-

216 treatment of pluripotent stem cells with ROCK inhibitor (-12h) strongly promoted mesoderm
217 differentiation. Co-treatment with ROCK inhibitor and CHIR reduced the effect, and addition of
218 ROCK inhibitor at +12hrs had no effect on differentiation (**Figure 3R-S**). We conclude that
219 reduced contractility primes pluripotent stem cells for specification but has no effect once
220 specification has been initiated by WNT activation.
221
222 <u>Hippo pathway and force-dependent WNT ligand secretion do not contribute to enhanced</u>
223 <u>mesoderm specification</u>
224 Mechanistically, how do changes in contractility impact cell fate specification? A major
225 target of mechanical force in epithelia is the Hippo pathway. YAP, a downstream effector of
226 Hippo signaling, has been previously associated with cell fate patterning in 2D gastruloids [34], and
227 substrate stiffness-driven mesoderm specification [35]. Low tension activates this pathway,
228 resulting in YAP phosphorylation and degradation. Conversely, high tension suppresses Hippo
229 signaling, blocking phosphorylation of YAP. The non-phosphorylated YAP translocates to the
230 nucleus to regulate gene expression. Surprisingly, however, phosphorylated YAP levels were not
231 affected during hiPSC differentiation or by cell relaxation (**Supplementary Figure 4A, B**). We
232 next directly probed for *CTGF* and *CYR61* expression, two well-described YAP target genes. Gene
233 expression strongly decreased during differentiation, as expected given the reported repressive
234 functions of YAP during mesendoderm specification [36], but expression level was not affected by
235 the cellular contractile status (**Supplementary Figure 4C**). Together, these data rule out a
236 significant role for the Hippo pathway in the acceleration of mesodermal differentiation
237 following cell relaxation.
238 Next, we investigated the positive feedback loop reported for BMP4-driven mesoderm
239 commitment, which relies on tension-dependent secretion of canonical WNT ligands [16]. We
240 treated our MYPT1^{CA}-NES-mNG cells with Doxycycline to trigger cell relaxation and probed for
241 canonical and non-canonical WNT ligands. As expected, expression of *TBX6* (a mesoderm
242 marker) increased in low contractile cells. Interestingly, canonical WNT ligand expression
243 (*WNT3A* and *WNT8A*) was strongly upregulated by suppression of contractility, while non-
244 canonical *WNT4* expression was unaffected by CHIR treatment or by relaxation (**Supplementary**
245 **Figure 4D**). To test whether increased *WNT3A/8A* expression was responsible for increased
246 mesoderm commitment in low-contractility cells, we blocked WNT ligand processing and

247 secretion using IWP-2, a Porcupine inhibitor. Addition of IWP-2 did not reverse mesoderm gene
248 expression in Y-27632-treated cells, suggesting that this pathway does not drive accelerated
249 mesoderm specification in response to cell relaxation (**Supplementary Figure 4E**). Together,
250 these data ruled out the involvement of two major pathways, previously thought to link cell
251 tension to mesoderm commitment [16,35] .
252
253 Intercellular adhesion and Adherens Junctions mediate cell contractility
254 Seeking a potential mechanism, we turned our attention to intercellular adherens
255 junctions (AJs). These junctions are under tension, generated by actomyosin interactions with
256 vinculin/α-catenin, which in turn are coupled to β–catenin and E-cadherin [37]. In addition,
257 tension across AJs is mediated by homotypic and calcium-dependent interactions between E-
258 cadherin molecules on adjacent cells [38]. As a major signaling hub, we reasoned that AJs might
259 transduce mechanical forces to impact cell fate specification. We first tested whether disrupting
260 AJs using EGTA (a calcium chelator) would affect cell specification. EGTA treatment caused
261 colony decompaction (**Figure 4A and Supplementary Fig 5A**), consistent with previous literature
262 linking AJ-disengagement with reduced force transmission [39,40]. Strikingly, EGTA treatment
263 triggered a strong enhancement of mesodermal and EMT marker expression (**Figure 4B-E and**
264 **Supplementary Figure 5B-C**). Knowing that reduced contractility mimics this phenotype, we
265 tested whether EGTA treatment would alter contractility. Staining for ppMLC2 confirmed that
266 EGTA treated cells are in a low contractile state (**Supplementary Figure 5D-E**).
267 As an orthogonal approach, we sought to uncouple force transmission from the
268 actomyosin network to E-cadherin via vinculin/α-catenin. To this end, we created α-catenin
269 knockdown (*CTNNA1* KD) hiPSCs, with a 50% decrease in protein expression (**Supplementary**
270 **Figure 5F-G**). First, because AJs are required for stemness acquisition during fibroblast
271 reprograming to iPSCs [41], we checked that the *CTNNA1* knockdown cells had not lost
272 pluripotency (**Supplementary Figure 5F, H-I**). Notably, ppMLC2 levels were 50% lower in the KD
273 cells (**Figure 4F-G**), confirming that α-catenin is a major contributor to cell actomyosin activity.
274 The *CTNNA1* KD hiPSCs exhibited higher and earlier expression of Brachyury. Strikingly, however,
275 these cells failed to further respond to Y-27632 treatment, while control cells responded as
276 expected by increasing Brachyury expression (**Figure 4H-I**). Together these data demonstrate

277 that AJ disruption reduces actomyosin contractility and that α-catenin-mediated force
278 transmission is a major determinant of mesoderm specification kinetics.
279
280 Junctional β-catenin localization scales with intrinsic actomyosin contractility in undifferentiated
281 hiPSCs
282 Our discovery of a key role for AJ mechanics in cell fate specification suggested that β-
283 catenin, which in epithelial cells is mostly bound to E-Cadherin at AJs, might respond to changes
284 in actomyosin contractility by modulating WNT signaling responsiveness. Release of β-catenin
285 from AJs, for example, might increase the cytoplasmic and nuclear pools to amplify expression
286 of *TBXT* and other mesoderm genes. Mechanosensitive functions for β-catenin during
287 development and tissue homeostasis have been described [16,42] but whether the junction-
288 associated and cytoplasmic β-catenin pools both contribute to WNT signaling is still
289 controversial [18], and other studies have suggested a connection in which increased junctional β-
290 catenin correlates with increased nuclear β-catenin [17] .
291 We hypothesized that loss of tension at AJs would release β-catenin to promote WNT-
292 responsive gene expression, and conversely that increased tension would promote binding at
293 AJs, thereby titrating out the free cytoplasmic/nuclear β-catenin. To test this mechanism,
294 undifferentiated hiPSCs were treated with either the Rho activator CN03 or ROCK inhibitor Y-
295 27632, causing an increase or decrease in ppMLC2, respectively (**Figure 5A-B and**
296 **Supplementary Figure 6A**). Strikingly, under each condition, junctional β-catenin levels
297 correlated closely with the level of active ppMLC2 in the cells (**Figure 5B-C and Supplementary**
298 **Figure 6B**). To rule out staining artifacts, we performed comparable experiments using our
299 EGFP-β-catenin knock-in hiPSC line (**Figure 5D**), with a similar conclusion (**Figure 5E-F,**
300 **Supplementary Figure 6C and Supplementary Video 2**). Importantly, overall β-catenin
301 expression is not affected by contractile state, suggesting that contractility does not regulate β-
302 catenin level but rather its localization (**Supplementary Figure 6D-F**). Together, these data
303 demonstrate that β-catenin association with AJs scales directly with actomyosin contractility.
304
305 Cell relaxation promotes nuclear β-catenin localization and occupancy at *TBXT* promoter
306 In the absence of WNT signaling, cytosolic β-catenin is maintained at a low level by
307 association with a destruction complex, where it is phosphorylated at Ser45 by CK1, which

308 primes the protein for subsequent phosphorylation by GSK3β, driving its ubiquitination and
309 degradation. WNT activation disrupts the destruction complex, permitting the accumulation of
310 stable, non-phosphorylated β-catenin, which can enter the nucleus to drive gene expression.
311 This "active" state can be assessed from the detection of non-phosphorylated Ser45 β-catenin.
312 To test for differential accumulation of active β-catenin, we isolated cytosolic and nuclear
313 fractions from cells that contain the Dox-inducible MYPT1^{CA}-NES-mNG construct
314 (**Supplementary Figure 7A**). Purity of each fraction was assessed for enrichment of a nuclear
315 and cytosolic marker, Lamin A/C and GAPDH, respectively (**Supplementary Figure 7B**).
316 Fractionation showed that active β-catenin was strongly enriched in both the cytosolic and the
317 nuclear fractions of cells treated with CHIR + Dox (24h) versus cells treated only with CHIR
318 (**Figure 6A-B**). Immunostaining confirmed the nuclear enrichment of active β-catenin (**Figure 6C**
319 **and Supplementary Figure 7C-D**) after 24h of differentiation in low contractile conditions.
320 We validated this observation by imaging endogenous mEGFP-β-catenin knock-in hiPSCs
321 treated with CHIR in either control or low contractile (+Y-27632) conditions. First, we noticed
322 nuclear accumulation of mEGFP-β-catenin within 5h of CHIR treatment, regardless of the
323 contractile status of the cells. However, while β-catenin signal decreased over time in vehicle-
324 treated cells, remaining visible after 20h in only a few nuclei, low contractile cells showed a
325 robust and enhanced nuclear localization (**Figure 6D-E and Supplementary Video 3**).
326 Finally, knowing that β-catenin is enriched in the nucleus upon low contractility, we
327 focused on the ability of β-catenin to interact with its binding partners and to regulate WNT-
328 responsive genes. Because of the timing of our phenotype, we ruled out an involvement of β-
329 catenin interactions with transcription factors (such as SOX family, SMAD, TBX3) [43,44], as they are
330 involved later during specification [45]. In addition, ChIP-seq experiments report that TCFs/β-
331 catenin binding is the main event during pluripotency exit and early specification [45,46].
332 Mammalian genomes encode four TCF proteins (TCF7, TCF7L1, TCF7L2 and LEF1), all of which
333 bind to similar DNA sequences [47], show redundant functions [46,48] and co-occupy similar DNA
334 regions [49,50]. TCF3 (encoded by *TCF7L1*) is the most highly expressed member in hiPSC
335 (**Supplementary Figure 7E**) but is widely reported to be repressive [51–54]. Therefore, we focused
336 on the second most highly expressed factor, TCF4 (encoded by *TCF4L2*). Nuclei isolated from Y-
337 27632-treated EGFP- β-catenin knock-in hiPSCs showed higher binding between β-catenin and
338 TCF4 compared to vehicle-treated cells (**Figure 6F-H**). Finally, CUT & RUN assays showed that

339 low contractility significantly increased β-catenin recruitment to *TBXT* promoter during
340 differentiation (**Figure 6I and Supplementary Figure 7F**), supporting a priming model. Together,
341 these findings suggest that the promotion of nuclear β-catenin accumulation by cytoskeletal
342 relaxation accelerates mesoderm program by binding to its TCF co-mediator. However, this
343 model can only hold true if the concentration of CHIR used in our study (7.5 μM) does not
344 saturate the β-catenin signaling response. To test this premise, we doubled the concentration of
345 CHIR and probed for expression of WNT target genes as a read-out for WNT signaling
346 (**Supplementary Figure 7G**). *LEF1* and *AXIN2* expression responded in a dose-dependent
347 manner to CHIR. Interestingly, however, at any given CHIR concentration, inhibition of cell
348 contractility further enhanced WNT-target gene responses.
349 Collectively, we demonstrate that actomyosin contractility regulates β-catenin
350 availability and that cell relaxation amplifies active β-catenin translocation to the nucleus
351 synergistically with CHIR to enhance mesoderm commitment (**Figure 7**).
352
353 **Discussion**
354 Here, we have identified an inverse relationship between actomyosin contractility and
355 mesoderm specification in hPSCs. Mechanistically, our data support a model in which adherens
356 junctions serve as dynamic reservoirs that sequester β-catenin away from the cytoplasmic
357 signaling pool. We propose that the inter-dependence of actomyosin contractility and AJs
358 creates a titration mechanism for β-catenin availability, thereby tuning mesoderm specification.
359 Previous papers have reported that, contrary to our observations, increased mechanical tension
360 promotes β-catenin-dependent mesoderm induction. For example, tension has been reported
361 to promote Brachyury expression in hESC [17], in Bilateria [55] and Cnidaria [20] , while in gastrulation-
362 like models of hESC, Muncie et al argued that high cell adhesion tension on compliant substrate
363 can promote mesoderm induction [16]. This study proposed a dual function for mechanical
364 tension. First, BMP4-driven Brachyury expression relies on mechanical stretch of cell junctions,
365 allowing destabilization of β-catenin from AJs and its nuclear translocation. Following this
366 initiation stage, a positive feedback loop reinforces mesoderm commitment through increased
367 WNT ligand secretion. Strikingly, on Matrigel-coated plates, we observe the opposite outcome.
368 Importantly, our unconstrained system directly focuses on contractility rather than tension
369 geometry or substrate properties. Our findings suggest that intrinsic contractility, even in

370 unpatterned settings, is sufficient to guide cell fate decisions. We provide causal and cell-
371 intrinsic evidence that actomyosin-generated forces act upstream of mesodermal fate, in the
372 pluripotent state, to inhibit cell specification. Second, our protocol directly activates WNT
373 signaling by inhibition of the destruction complex, as do WNT ligands, in contrast with the
374 indirect effects of BMP4 activation. Importantly, a previous study showed that epithelial
375 cohesiveness and tight junctions block access by BMP4 to its receptor on the lateral plasma
376 membrane [56]. Therefore, BMP4 signaling can only activate Brachyury expression at colony edges
377 and corners [16]. However, our protocol uses a cell-permeable small molecule inhibitor as the
378 differentiating cue, circumventing this diffusion barrier. Third, our findings distinguish our model
379 from alternative force-mediated mechanisms such as Hippo/YAP signaling [35] or tension driven
380 WNT ligand secretion [16], neither of which accounted for the enhanced mesoderm specification.
381 One explanation might be that pluripotent stem cells are insensitive to Hippo activation because
382 of their inability to perceive cell-cell interactions, as previously reported [35]. Finally, our system
383 relies on activating or reducing contractility at the pluripotent state by pre-treating cells prior to
384 differentiation and maintaining treatment during cell commitment. We observed a timing-
385 dependent response during which enhanced mesoderm identity was only achieved following
386 ROCK inhibition pre-treatment of cells in the pluripotent state. Therefore, our study suggests
387 that low contractility primes pluripotent cells to enter the differentiation trajectory. Such a
388 licensing mechanism would likely involve cis-regulatory element-mediated chromatin priming
389 that can potentiate gene activity prior to specification events [57]. Alternatively, we note that
390 actomyosin-dependent epigenome regulation was previously associated with RNA-polymerase
391 II activity and lineage commitment in adult stem cells [58].
392 We here describe a titration mechanism by actomyosin contractility that allows a
393 synchronization with developmental processes during cell commitment. β-catenin exists in two
394 pools, one bound to the adherens junctions through E-cadherin and one cytosolic pool that is
395 central to WNT signaling. The regulation and exchange of β-catenin molecules between these
396 two pools remains poorly understood. E-cadherin binding to β-catenin prevents its nuclear
397 translocation and transcriptional co-activator function [19]. Src-mediated phosphorylation of β-
398 catenin at residue Y654 has been reported to reduce binding to E-cadherin [59], so one possibility
399 might be that Src tyrosine kinase activity is anti-dependent on contractility in pluripotent stem
400 cells. Alternatively, however, Gayrard et al [21] reported an inverse mechanism through which, in

401 migrating cells, Src-dependent phosphorylation of FAK causes actin remodeling and E-cadherin
402 tension relaxation, resulting in the release and nuclear translocation of β-catenin. In our system,
403 reduced tension causes loss of β-catenin from AJs, accumulation in the cytosolic compartment,
404 and translocation into the nucleus. Finally, in *Xenopus*, decreased ROCK-dependent actomyosin
405 contractility promotes an ectoderm-to-mesoderm transition, suggesting force-dependent
406 lineage plasticity is a conserved mechanism [60]. While we have not tested for alternative cell fate
407 following CHIR addition, our differentiation protocol was adapted from Lian et al [12,13] and was
408 not reported to lead to ectodermal identity.
409

410 **Acknowledgements**

411 We thank Cynthia Reinhart-King for giving us access to the QPOL facility. We thank the Weaver
412 lab (UCSF) and the Gardel lab (University of Chicago) for sharing the T-mNG knock-in hESC line.
413 We thank Dr. Vivian Gama lab (Vanderbilt University) for providing the NSC lysate, Pax6 and
414 Otx1/2 antibodies. We also thank all members of the Macara lab, especially Dr. Christian de
415 Caestecker for valuable suggestions and advice. This work was funded by an American Heart
416 Association postdoctoral fellowship (Award ID 23POST1018347 to L.F.), a 2024 Vanderbilt
417 Mechanobiology fellowship (to L.F.), a 2024 and 2025 Vanderbilt Mechanobiology fellowship (to
418 L.F.) and a grant from the National Institutes of Health (GM070902 to I.G.M.).
419

420 **Author contributions**

421 L.F. conceived the study, performed and quantified all experiments except the ones stated
422 below, and wrote the manuscript. V.V. performed the CUT & RUN assay. W.W. imaged and
423 quantified the QPOL data. I.G.M. supervised the project, and edited the manuscript.
424

425 **Data availability statement**

426 The data are available from the corresponding author upon reasonable request.
427

428 **Declaration of interest**

429 The authors declare no competing interests.
430
431

432 **Material & Methods**

433 Research compliance and ethical regulation

434 All experiments using human ESCs were performed using the WA09 (H9) cell line under the
435 supervision of the Vanderbilt Institutional Human Pluripotent Cell Research Oversight
436 Committee (protocol IRB no. 160146). No cells were sourced directly from human embryos.

437

438 Reagents

439 Common laboratory reagents used in this study are listed in Supplementary Table 1

440

441 Cell culture and maintenance

442 Human GM25256 iPSCs were obtained from the Coriell Institute. The mEGFP–CTNNB1 knock-in
443 GM25256 iPSC cell line was obtained from the Allen Cell Collection, Coriell Institute (cell ID
444 AICS-0058-067). The human ESC line H9 (WA09) was obtained from the WiCell Research
445 Institute. The T-mNG knock-in hESC H9 was made by Valerie Weaver lab (UCSF) and kindly
446 provided by Margaret Gardel (University of Chicago). The iPSC and ESC H9 lines were cultured
447 on Matrigel-coated six-well plates (Matrigel diluted at 42 µg ml−1 in DMEM/F12 medium) and
448 cultured in mTeSR1 medium. The medium was changed daily until the cells reached 70%
449 confluency. Cells were passaged using Gentle cell dissociation reagent for 4 min, resuspended in
450 mTseR1 medium as small clusters and replated at 1:7. HEK293T cells were obtained from the
451 ATCC. Cells were grown in 10% FBS DMEM medium and passaged at 1:10 every 2-3 days.
452 All cell lines used in this study were maintained at 37 °C under 5% CO2.

453

454 Cell freezing and thawing

455 Human iPSCs and ESCs were harvested from culture dishes using Gentle cell dissociation
456 reagent and centrifuged at 120g for 3 min. The pellets were resuspended in mTeSR1 medium
457 supplemented with 10% DMSO and aliquoted into cryovials. Cells were first transferred to
458 −80 °C for 24 h before long-term storage in liquid nitrogen. iPSCs and ESCs were slowly thawed
459 using mTeSR1, centrifuged and resuspended in mTeSR1 supplemented with 10 µM Y-27632 for
460 24 h.

461

462 Mesoderm differentiation protocol and drug treatments

463 Differentiation was initiated when cells reach 70-80% confluency. Cells were treated with 7.5
464 µM CHIR99021 (hereafter CHIR) diluted in RPMI media supplemented with 1X B27 minus insulin
465 and 100U/mL Penicillin and 100 µg/mL streptomycin (1X).
466 For pharmaceutical inhibition of contractility, cells (50% confluent) were pre-treated overnight
467 or 3h with drug or vehicle diluted in mTeSR1. Differentiation was initiated the day after (cells
468 reached 70-80% confluent) by switching to CHIR media as described above, supplemented with
469 the drug or vehicle. For MYPT1^{CA}, cells were pre-induced overnight with Doxycycline or vehicle
470 (water) diluted in mTeSR1 before initiating the differentiation protocol in the presence of
471 Doxycycline or water.
472 For pharmaceutical stimulation of cell contractility, 70-80% confluent cells were pre-
473 treated for 3h with 4 µg/mL CN03 or water in mTeSR1, followed by CHIR treatment
474 supplemented with CN03 or water. For EGTA treatment, 70-80% confluent cells were pre-
475 treated for 30min with 1mM of EGTA or water in mTeSR1, followed by CHIR treatment
476 supplemented with 10 µM EGTA or water. For concentration of each drug, please refer to
477 Supplementary Table 1.
478
479 Lentiviral preparation
480 HEK293T were grown at 40% confluency in 10 cm plate and transfected using Calcium-
481 Phosphate. Briefly, 20 µg of lentiviral plasmid, 15 µg of pSPAX2 (Addgene #8454) and 6 µg
482 pMD2G (Addgene #12260) were mixed with 450 µL sterile water and 50 µL of 2.5M $CaCl_2$
483 solution, previously filter sterilized. DNA mixture was added dropwise into 500 µL of 2X HeBS
484 (50 mM HEPES, 10 mM KCl, 12 mM dextrose, 280 mM NaCl and 1.5 mM Na2PO4, pH 7.04) with
485 constant vortexing. Solution was added dropwise on HEK 293T cells for 6h. Medium was
486 replaced with 8mL of fresh 10% FBS DMEM medium for 48h. Supernatant was filtered through a
487 0.22 µm membrane and concentrated using a 100kDa cut-off Amicon centrigal unit. Aliquots
488 were frozen at -80 °C.
489 For generation of CRISPR cells, single-guide RNA was selected using Benchling design
490 tool, and are listed in Supplementary Table 3. Annealed oligonucleotides were cloned into
491 pLentiCrispRv2-Puro as described by Sanjana and colleagues
492 (https://doi.org/10.1038/nmeth.3047). Lentiviral particles were prepared as described above.

493 hiPSCs were transduced in suspension and selected 48h post-transduction using 1 µg/mL of
494 Puromycin.
495
496 SDS-PAGE and Western blotting
497 Cells were washed with ice cold 1X PBS and lysed with 70 µL RIPA buffer (150 mM NaCl, 10 mM
498 Tris–HCl pH 7.5, 1 mM EDTA, 1% Triton X-100, 0.1% SDS) supplemented with and 1X protease
499 and phosphatase inhibitors. Mechanical disruption was performed by scrapping the cells off the
500 plate, transferring the lysate into a 1.5mL Eppendorff tube and vortexing for 5 seconds followed
501 by 5 min incubation on ice. Soluble proteins were collected by centrifugation at 16000 g (13200
502 rpm) for 10min at 4°C. Protein concentration was measured using Precision Red following the
503 manufacturer's instructions. Lysates in sample buffer were boiled for 5min.
504 For ppMLC blotting, cells were washed with 1X PBS and directly lysed using 250 µL of
505 boiling 1X sample buffer. Lysates were sonicated 3 times for 10 seconds with 60 seconds
506 incubation on ice between each blast. 30 µg of proteins were resolved on 1.5mm thick bis-tris
507 acrylamide gels and transferred onto 0.2 µm nitrocellulose membrane using BioRad wet transfer
508 system (50 V for 2hours). Membranes were blocked for > 30min at room temperature (RT) with
509 5% BSA in 1X TBS-T (10 mM Tris pH 8.0, 150 mM NaCl and 0.5% Tween 20) and incubated
510 overnight at 4°C and gentle rocking with primary antibodies diluted in blocking buffer
511 (Supplementary Table 2). Membranes were washed 3 times with 1X TBS-T and incubated for 1h
512 at RT with AlexaFluor-conjugated secondary antibodies (Supplementary Table 2). After 3
513 additional washes in 1X TBS-T, membranes were scanned using Li-Cor Odyssey CLx system,
514 analyzed and processed using Image StudioLite v. 5.2.
515
516 Immunofluorescence
517 Cells were cultured on Matrigel-coated Ø 12mm coverglass, fixed with 4% paraformaldehyde for
518 10min, permeabilized for 5min at RT (20mM Glycine, 0.05% Triton X-100 in 1X PBS), and
519 incubated with blocking buffer for > 30min (5% BSA in 1X PBS). Coverslips were transferred into
520 a dark humidified chamber and incubated with primary and AlexaFluor-conjugated secondary
521 antibodies (Supplementary Table 2) diluted in blocking buffer for 2 hours. Coverslips were
522 washed in 1X PBS and mounted on glass slide using Fluoromount-G mounting solution.
523 For ppMLC staining, samples were incubated overnight with primary antibody.

524

525 Image acquisition, analysis and processing

526 Micrographs were obtained using an inverted Nikon A1-R confocal microscope equipped with a
527 x20 objective (Numerical aperture NA 0.75), a x40 oil objective (NA 1.20) and a x100 oil
528 objective (NA 1.40). Z-stacks covering the entire cell height were acquired. Maximum Intensity
529 (MaxIP) Projections were obtained and images were analyzed and processed using Fiji (version
530 2.1.0/1.54f). Images processing did not include a denoising step except for Supplementary
531 Video 3.

532

533 MYPT1^{CA}-NES-mNeonGreen cloning strategy and cell line generation

534 A gBlock was obtained from IDT, corresponding to truncated human MYPT1 (aa 1-300) in fusion
535 with a PKI super Nuclear Export Signal and mNeonGreen sequence. The gBlock was amplified
536 using Fusion polymerase and the following primers: Fwd 5'-
537 CTGCTGACCGGTACCATGGCGGACGCGAAGC-3' and Rev 5'-CATCATACGCGTCTACGATCCGCCACCGC-
538 3'. PCR product and recipient backbone (pInducer10b-HA-KRas G12V Addgene #164928) were
539 digested with AgeI-HF and MluI-HF for 1h at 37°C, gel purified, and ligated overnight at 16°C
540 using T4 ligase. Ligation reactions were transformed into chemically competent E.Coli Stbl3
541 strain and selected on Ampicillin plates. Plasmids were isolated from single colonies (QIAprep
542 Spin MiniPrep kit). The presence of the insert was confirmed by restriction digestion. Positive
543 clones were sent for full plasmid sequencing provided by Genewiz Plasmid-EZ service before
544 plasmid purification using Takara Bio NucleoBond XtraMidi kit. WT hiPSCs were transduced as
545 described above and cells were selected 48h later with 1 µg/mL of Puromycin.

546

547 Quantitative Polariztion Microscopy (QPOL)

548 The contractility of cells was measured using quantitative polarization microscopy (QPOL) as
549 described previously [33]. Briefly, QPOL was built on an inverted Axiovert microscope equipped
550 with an Axiocam 506 color camera. A motorized linear polarizer (Thorlabs, Newton, NJ) and a
551 circular polarizer were positioned in the illumination plane above the condenser and in the
552 imaging plane, respectively. Images were captured using a 20x/0.5 N.A. polarization objective.
553 For each field of view, image sequences were acquired with 10° intervals of the rotating
554 polarizer over the range of 0–180° using Zen software. The polarized image sequences were

555 then processed using a custom MATLAB code to generate pixel-by-pixel retardance maps. The
556 obtained retardance images then underwent background subtraction and subsequent analysis
557 with ImageJ. The retardance signal proportional to cell contractility was quantified as the
558 average value of the background-subtracted retardance over the cell area.
559
560 Flow cytometry analysis
561 T-mNeonGreen knock-in hESC were transduced with a lentivector expressing Histone 2B-
562 mScarlet (pWPI-H2B-mScarlet). Cells were pre-treated overnight with Vehicle (water) or 10 µM
563 Y-27632. Differentiation was initiated for 24 hrs as described above and cells were harvested as
564 single cells. Briefly, cells were washed and gentle cell dissociation buffer was added for 8 min at
565 37°C. Cell suspension was centrifuged and resuspended in 500 µL PBS. Cells were passed
566 through a Ø 40 µm strainer directly into 500 µL of 8% PFA (final concentration 4%) and fixed for
567 10 min on a wheel before sending them for cytometry using a 5-laser Fortessa analyzer (70 µm
568 nozzle). Singlets were selected based of forward and side scatter. mScarlet (PE-Texas-RedA) and
569 mNeonGreen (GFP-A) population were selected by drawing a gate on double negative WT hESC
570 shifted by one order of magnitude. Percentage of mNeonGreen/mScarlet double positive was
571 reported using the online flow cytometry analysis resource https://floreada.io.
572
573 RNA isolation and RT-qPCR
574 Cells were washed and RNAs were isolated using RNeasy mini kit following manufacturer's
575 instructions. 1 µg of RNA was reverse transcribed to cDNA using the SuperScript III first-strand
576 synthesis kit. cDNA was diluted 1:5 in water and mixed with Maxima SYBR Green/1mM of each
577 primer (Supplementary Table 3). Quantitative PCR was performed on a BioRad CFX96
578 thermocycler with thermal cycling conditions as followed: Initial denaturation: 95°C for 10 min
579 followed by 40 cycles of denaturation at 95°C for 15 sec, annealing at 58°C for 30 sec, extension
580 at 72°C. Final step was performed for 10 sec at 95°C. C_t values from technical triplicates were
581 averaged and normalized to GAPDH using the $\Delta\Delta C_t$ formula.
582 TCF expression levels (Supplementary Figure 7E) were curated from the transcriptomic data
583 available on the Allen Institute website (https://www.allencell.org/genomics.html).
584
585 Cell Fractionation

586 Following appropriate treatment, cells were washed with ice cold 1X PBS and collected as single
587 cell suspension using gentle cell dissociation as previously described. Cell suspension was
588 washed with cold 1X PBS and resuspended in 500 µL of cold PBS. 100 µL of the cell suspension
589 was set aside and mixed with 30 µL of 4X sample buffer. Samples were sonicated for 15 sec at
590 20% power 3 times, boiled 5min and stored at -20 °C (Whole Cell Lysate fraction or WCL).
591 Cell fractionation was performed using Cell signaling kit (#9038) and their protocol. Briefly, the
592 remaining 400 µL of cell suspension was centrifuged at 500 x g at 4°C for 5min. Supernatant was
593 removed and pellet was resuspended in 250 µL of CIB buffer, vortexed for 5 sec and incubated
594 on ice for 5 min. Samples were centrifuged at 500 x g at 4°C for 5min and supernatant was
595 stored in pre-chilled tube (= Cytoplasmic fraction). Pellet was resuspended in 250 µL of MIB
596 buffer, vortexed for 15 sec and incubated on ice for 5 min. Samples were centrifuged at 8000 x g
597 at 4°C for 5min and supernatant was discarded (= Membrane and organelle fraction). Pellet was
598 resupended in 125 µL of CyNIB buffer, sonicated for 5 sec at 20% power 3 times (cytoskeletal
599 and nuclear fraction). Each fraction was mixed with the appropriate volume of 4X sample buffer
600 to obtain a final concentration of 1X. Samples were boiled for 5min and centrifuged before
601 loading 15 µL.
602
603 Nuclear extraction and CUT & RUN Assay
604 Nuclei extraction: 500,000 cells (per sample) were harvested using TrypLE, washed with
605 1X PBS, and centrifuged at 600 × g for 3 min at RT. The pellet was resuspended in Nuclear
606 Extraction (NE) buffer (20 mM HEPES, pH 7.9, 10 mM KCl, 0.1% Triton X-100, 20% glycerol, 1 mM
607 $MnCl_2$, 0.5 mM spermidine, 1X Roche Complete Protease Inhibitor EDTA-Free) and incubated for
608 10 min at 4 °C. After incubation, samples were centrifuged at 600 × g, and the isolated nuclei
609 were resuspended in 100 µL of NE buffer per sample. Nuclei were incubated with 10 µL of
610 magnetic Concanavalin A beads for 10 min at RT to facilitate binding.
611 DNA purification: Bead-bound nuclei were incubated with 3 µL of anti-β-catenin
612 antibody in 50 µL of digitonin buffer (20 mM HEPES, pH 7.5, 150 mM NaCl, 0.5 mM spermidine,
613 0.01% digitonin, 1X Protease Inhibitor Cocktail) containing 2 mM EDTA overnight at 4 °C.
614 Following incubation, samples were washed twice with digitonin buffer and resuspended in 50
615 µL of the same buffer supplemented with 1.5 µL of pAG-MNase. Samples were incubated for 10
616 min at RT, followed by two additional washes, and subjected to chromatin digestion at 4 °C for 2

617 hrs with 2 mM $CaCl_2$. To quench the reaction, 33 µL of STOP buffer (340 mM NaCl, 20 mM EDTA,
618 4 mM EGTA, 50 µg/mL RNase A, 50 µg/mL glycogen) was added, followed by incubation at 37 °C
619 for 10 min. Beads were collected using a magnetic rack, and the supernatant containing
620 released DNA was transferred to a new tube. DNA was purified using DNA purification buffers
621 and spin columns following the manufacturer's instructions and eluted in 30 µL of buffer
622 qPCR reaction & Data analysis: Reactions were prepared using 1 µL of purified DNA from
623 the CUT and RUN, with 2 µL Forward and reverse primer mix (5 µM each), 5 µL SYBR Green
624 master mix (Applied Biosystems), and 2 µL of nuclease-free water. Thermal cycling condition
625 were set up on a BioRad CFX96 thermocycler as followed: Initial denaturation: 95°C for 10 min
626 followed by 40 cycles of denaturation at 95°C for 15 sec, annealing at 60°C for 30 sec, extension
627 at 72°C. Final step was performed for 10 sec at 95°C. Ct values from technical triplicates were
628 averaged, and ΔCt was calculated by subtracting Ct IgG control from target. Fold enrichment
629 was calculated using the ΔΔCt method: Fold enrichment=$2^{-\Delta\Delta Ct}$.
630
631 GFP-Trap immunoprecipitation
632 EGFP-CTNNB1 knock-in hiPSCs were harvested using TripLE and nuclei were isolated as
633 described above. For each reaction, two wells were collected. Both 0h and 24h nuclei were
634 cryopreserved by slowly freezing them in NE buffer using an isopropanol-filled chiller at -80°C.
635 Nuclei were quickly thawed using a 37°C water bath, centrifuged at 600 x g and resuspended
636 using 100 µL of lysis buffer (10 mM Tris/HCl pH 7.5, 150 mM NaCl, 0.5 mM EDTA, 0.5 % NP40).
637 Nuclear lysates were incubated 5 min on ice and cleared by centrifugation (16000 x g for 10 min
638 at 4°C. Soluble protein concentration was measured using Precision Red following the
639 manufacturer's instructions and pellets were mixed with 1X sample buffer (insoluble fraction).
640 Meanwhile, GFP-Trap beads (20 µL/reaction) were equilibrated three times with 500 µL of ice-
641 cold dilution buffer (10 mM Tris/HCl pH 7.5, 150 mM NaCl, 0.5 mM EDTA). 150-200 µg of soluble
642 proteins were prepared in 500 µL of ice-cold dilution buffer and mixed with equilibrated GFP-
643 Trap beads. Reactions were incubated for 2 hrs at 4°C on a wheel. Beads were then pelleted
644 (2500 x g, 3min at 4°C) and washed three times with 500 µL of ice-cold wash buffer (10 mM
645 Tris/HCl pH 7.5, 150 mM NaCl, 0.05 % NP40, 0.5 mM EDTA). Proteins were eluted by adding 50
646 µL of 2X sample buffer and boiled for 5 min. Eluted proteins were resolved by western blot as

647 described above. TCF4 binding was measured by densitometry of the TCF4 band (prey)
648 normalized to the GFP band (bait).
649
650 Reproducibility and statistics
651 All datasets were analyzed using GraphPad Prism10 (version 10.0.3). Individual measurements
652 (n) were averaged for each biological repeat (N). Datasets were tested for normality (Shapiro-
653 Wilk test for normality of biological replicates) before applying the appropriate statistical test on
654 the biological repeats (N), except if mentioned differently in the figure legend. Error bars
655 represent S.D. except where stated otherwise. For datasets displayed as superplots, individual
656 measurements and biological repeats are represented by small and large dots respectively.
657 Violin plots display median (thick dotted line) and quartiles (thin dotted lines). Each dataset for
658 a biological repeat is color coded. Significance levels are given as follows and exact p-values are
659 indicated in each figure: n.s., not significant ($p \geq 0.05$); *$p < 0.05$; **$p < 0.01$; ***$p < 0.001$; and
660 ****$p < 0.0001$.
661 All experiments, including representative MaxIPs and western blots, were performed at
662 least three times independently as biological repeats, unless stated otherwise in the legends.
663 No statistical method was used to pre-determine the sample size, the experiments were not
664 randomized and the investigators were not blinded to allocation during experiments and
665 outcome assessment.
666
667 **Figure legends**
668 Figure 1: Increased actomyosin contractility is sufficient to block mesoderm commitment and
669 EMT
670 (A) Experimental design for co-culture experiment. hiPSC were transduced with lentivector
671 expressing ROCK2^{CA} or MLCK^{CA}. mVenus positive-transduced cells were mixed with mVenus-
672 negative WT hiPSCs. ROCK2^{CA}/MLCK ^{CA} expression is induced by addition of Doxycycline 24h
673 prior to initiating mesoderm differentiation. Doxycycline induction was maintained during the 3
674 days of differentiation using CHIR before fixing and staining.
675 (B-H) Representative MaxIP immunofluorescence for Brachyury (B), EOMES (D), Slug (F) and ZO-
676 1 (H) in Vehicle and Doxycycline-induced ROCK2^{CA} co-culture. mVenus-positive cell clusters are
677 highlighted by an orange dotted line. Individual channels are presented as inverted LUT. Scale

678 bar = 50 µm. For (H), magnified mVenus-positive and mVenus-negative areas are shown as
679 insets. Scale bar = 20 µm. Quantification of Brachyury (C), EOMES (E) and Slug-positive cells (G)
680 is reported as violin plot, comparing mVenus-positive *vs* mVenus-negative clusters in the
681 presence or absence of Doxycycline. Median (Plain red line) and quartiles (Dotted black lines).
682 For Brachyury, n = 7 (+ Veh) and n=15 (+ Dox) across N=3 independent biological repeats. For
683 EOMES, n=9 across N=3 independent biological repeats. For Slug, n=9 (+ Veh) and n=10 (+ Dox)
684 across N=3 independent biological repeats. One-way ANOVA with Tukey's multiple comparisons
685 post-test was performed.
686
687 <u>Figure 2: Genetic inhibition of actomyosin contractility promotes hiPSC conversion to the</u>
688 <u>mesoderm lineage</u>
689 (A) Summary of the main regulators of MLC phosphorylation.
690 (B) Schematic representation of full length human MYPT1 (1030 aa), interacting with PP1c
691 phosphatase and a protein of unknown function M20. Truncation of MYPT1 Cterm Δ301-1030
692 leads to a constitutive recruitment and activation of PP1C. Truncated MYPT1 was fused with
693 NES-mNeonGreen and is referred to as MYPT1^{CA}-NES-mNG.
694 (C) Immunoblot of phospho T18/S19 MLC2 (ppMLC2) and total MLC2 in WT hiPSCs treated with
695 Doxycycline or hiPSC expressing MYPT1^{CA}-NES-mNG in the presence or absence of Doxycycline.
696 α-Tubulin was used as loading control. Molecular weights (M.W.) are displayed on the right side.
697 (D, E) – Representative MaxIP immunofluorescence of hiPSC expressing MYPT1^{CA}-NES-mNG and
698 treated or not with Doxycycline. Cells were fixed and stained for phospho T18/S19 MLC2
699 (ppML2 - Magenta), DNA (blue) and tight junction marker ZO-1 (Orange). Scale bar = 50 µm (D).
700 Fraction of the cellular area positive for ppMLC2 following Doxycycline induction of MYPT1^{CA}-
701 NES-mNG hiPSC and reported as violin plots. Median (Plain red line) and quartiles (Dotted black
702 lines). n=32 technical repeats across N=3 independent biological repeats. Two-tailed unpaired t
703 test was performed on the biological repeats (E).
704 (F) Experimental design. hiPSC cells were transduced with pInducer20-MYPT1^{CA}-NES-mNG and
705 stable population was selected with puromycin. MYPT1^{CA} cells were treated or not with
706 doxycycline for 16h and treated with CHIR supplemented or not with doxycycline. Parental WT
707 line was differentiated with Doxycycline.

708 (G, H) Representative immunoblot for Brachyury (mesoderm marker), Snail and Slug (EMT
709 markers) using WT and MYPT1^{CA}-NES-mNG hiPSCs, following CHIR treatment (0h-48h) in the
710 presence or absence of Doxycycline, as shown in (F). Molecular weights (M.W.) are displayed on
711 the right side (G). Brachyury expression was quantified by densitometry and normalized to α-
712 Tubulin as loading control across N=3-4 independent biological repeats. Mean and S.D. are
713 displayed. A one-way ANOVA with Tukey's multiple comparisons post-test was performed (H).
714 (I) Immunoblot of PARP (cell death marker) and Brachyury (Mesoderm marker) during
715 mesoderm commitment (0hr-48hrs CHIR) using MYPT1^{CA}-NES-mNG hiPSCs induced +/
716 Doxycycline, as shown in (F). Molecular weights (M.W.) are displayed on the right side.
717 (J, K) Representative MaxIP immunofluorescences of WT and MYPT1^{CA}-NES-mNG hiPSCs treated
718 with CHIR for 24h +/- Doxycycline as shown in (F). Cells were stained for nuclei (DNA), EMT
719 marker (ZO-1 – Inverted LUT) and Mesoderm marker (T/Bra – Inverted LUT). Scale bar = 100 µm
720 (J). Quantification of Brachyury expression is presented as violin plots. Median (Plain red line)
721 and quartiles (Dotted black lines). n=15-16 technical repeats across N=3 independent biological
722 repeats. One-way ANOVA with Šidák's multiple comparisons post-test was performed on
723 biological repeats (K).
724
725 <u>Figure 3: Pharmaceutical inhibition of actomyosin contractility promotes hiPSC and hESC</u>
726 <u>conversion to the mesoderm lineage</u>
727 (A) Experimental design. WT hiPSCs or hESCs were pre-treated overnight with small molecules
728 to lower contractility, followed by differentiation.
729 (B) Immunoblot of Brachyury during hiPSC-to-mesoderm commitment (0-48h) in the presence
730 (+ Y-27632) or absence (+ Veh) of ROCK inhibitor, as shown in (A). Molecular weights (M.W.) are
731 displayed on the right side.
732 (C) Brachyury expression was quantified by densitometry and normalized to α-Tubulin as
733 loading control across N=3 independent biological repeats. Mean and S.D. are displayed. Two-
734 tailed unpaired t test was performed.
735 (D - G) Relative expression of mesoderm markers (*MESP1, TBX6*) (D, E) and EMT markers
736 (*SNAI1, SNAI2*) (F, G) 48h post CHIR treatment in the presence (+Y-27) or absence (+Veh) of
737 ROCK inhibitor as shown in (A). N=3 independent biological repeats except for *MESP1* N=4

738 independent biological repeats. Mean and S.D. are displayed. Two-tailed unpaired t test was
739 performed.
740 (H) – Representative MaxIP immunofluorescences during hiPSC-to-mesoderm commitment (0-
741 48h) in the presence (+ Y-27632) or absence (+ Veh) of ROCK inhibitor as shown in (A). Cells
742 were stained with a nuclear marker (DNA), EMT marker (ZO-1 – Inverted LUT) and Mesoderm
743 marker (T/Bra– Inverted LUT). Scale bar = 50 µm.
744 (I, J) Quantification of Brachyury expression (I) and ZO-1 intactness (J) is represented as violin
745 plots with individual measurements (small dots) averaged for each biological repeat (large dots).
746 Median (Plain red line) and quartiles (Dotted black lines). n=10-15 technical repeats across N=3
747 independent biological repeats. One-way ANOVA with Tukey's multiple comparisons post-test
748 was performed on biological repeats.
749 (K, L) Analysis of Brachyury expression by flow cytometry following 24h CHIR treatment in the
750 presence (+Y-27632) or absence (+Veh) of ROCK inhibitor, as shown in (A), using Bra-
751 mNeonGreen knock-in H9 hESC line (K). Quantification of the percentage of mNeonGreen-
752 positive cells from N=4 independent biological repeats. Mean and S.D. are displayed. Two-tailed
753 unpaired t test was performed (L).
754 (M, N) Representative MaxIP immunofluorescence of hiPSCs treated with a MLCK inhibitor (ML-
755 7) or Vehicle (DMSO), as shown in (A). Cells were stained for nuclei (DNA) and phospho T18/S19
756 Myosin Light Chain 2 (ppMLC2 – Inverted LUT). Scale bar = 50 µm. Magnified views of the yellow
757 dotted ROI are shown for ppMLC2. Scale bar = 20 µm (M). Percentage of cellular area positive
758 for ppMLC2 following Vehicle or ML-7 treatment is reported as violin pots. Median (Plain red
759 line) and quartiles (Dotted black lines). n=15 technical repeats across N=3 independent
760 biological repeats. Two-tailed unpaired t test was performed on the biological repeats (N).
761 (O, P) Immunoblot of Brachyury (mesoderm) and PARP (cell death marker) using hiPSCs in the
762 presence (+ ML-7) or absence (+ Veh) of MLCK inhibitor at basal state (0h) and during CHIR
763 treatment (24hrs, 48hrs), as shown in (A). Cells treated with CHIR and Q-VD (Caspase inhibitor)
764 for 48hrs were used as control for PARP immunoblot. Molecular weights (M.W.) are displayed on
765 the right side (O). Brachyury expression was quantified by densitometry and normalized to α-
766 Tubulin as loading control across N=3 independent biological repeats. Mean and S.D. are
767 displayed. Mann-Whitney test was performed for the 24hrs timepoints and two-tailed unpaired
768 t test was performed for the 48hrs timepoints (P).

769 (Q) Experimental design. Effects of Y-27632 was tested at different time along the mesoderm
770 commitment. ROCK inhibitor was added 12h before differentiation (-12h), at the time of
771 differentiation (0h) or 12h after differentiation (+12h). All conditions were collected 24h post
772 differentiation.
773 (R, S) Representative immunoblot for Brachyury following addition of Vehicle or Y-27632 as
774 shown in (Q). Molecular weights (M.W.) are displayed on the right side (R). Brachyury expression
775 was quantified by densitometry and normalized to α-Tubulin as loading control across N=3
776 independent biological repeats. Mean and S.D. are displayed. Two-way ANOVA with Šidák's
777 multiple comparisons post-test was performed (S).
778
779 Figure 4: Adherens junctions disengagement promotes mesoderm fate
780 (A) Experimental design. hiPSCs were pre-treated with an acute concentration of EGTA to
781 disrupt calcium-dependent E-Cadherin junctions. Following pre-treatment, hiPSCs were
782 differentiated in the presence of a lower concentration of EGTA.
783 (B-E) Representative immunoblot of hiPSCs treated as shown in (A) and probed for Brachyury
784 (mesoderm marker), Snail and Slug (EMT markers) and Pax6 and Otx1/2 (Neuroectoderm
785 markers as negative controls). Neural Stem Cell (NSC) lysate was used as positive control for
786 Pax6 and Otx1/2. Non-specific band is designated by an asterisk. Molecular weights (M.W.) are
787 displayed on the right side (B). Expression of Brachyury (C), Snail (D) and Slug (E) was quantified
788 by densitometry and normalized to α-Tubulin across N=3 independent biological repeats. Mean
789 and S.D. are displayed. One-Way ANOVA with Šidák's multiple comparisons post-test was
790 performed.
791 (F, G) Representative immunoblot of control (Ctr) and α-catenin knockdown hiPSC lines at basal
792 state and probed for total and phospho-MLC2. Molecular weights (M.W.) are displayed on the
793 right side (F). Quantification of active MLC2 (ppMLC2/MLC2) was measured by densitometry
794 across N=3 independent biological repeats. Mean and S.D. are displayed. One-Way ANOVA with
795 Dunnett's multiple comparison post-test was performed (G).
796 (H, I) Representative immunoblot of control (Ctr) and α-catenin knockdown (*CTNNA1* KD #1 and
797 #2) hiPSC lines, differentiated for up to 48hrs in the presence or absence of ROCK inhibitor Y-
798 27632 and probed for α-catenin, Brachyury and α-Tubulin as loading control. Molecular weights
799 (M.W.) are displayed on the right side (H). Normalized Brachyury expression was measured by

800 densitometry across N=3 independent biological repeats. Mean and S.D. are displayed. One-
801 Way ANOVA with Šidák's multiple comparisons post-test was performed (I).
802
803 Figure 5: Contractility differentially regulates β-catenin localization at adherens junctions
804 (A) Experimental design
805 (B) Representative immunofluorescence of fixed hiPSCs treated with Vehicle, 4µg/mL CN03 or
806 10 µM Y-27632 for 3h and stained for ppMLC2 and β-catenin (inverted LUT), as shown in (A).
807 Scale bare = 50 µm.
808 (C) Linear regression analysis of junctional β-catenin and cellular ppMLC2 was quantified across
809 N=3 independent biological repeats (representing n=16 for Vehicle, n=19 for CN03 and n=17
810 technical repeats for Y-27632). R^2 value is reported.
811 (D) Experimental design
812 (E, F) Representative still pictures from mEGFP-β-catenin knock-in (KI) hiPSCs treated with
813 Vehicle, 4µg/mL CN03 or 10 µM Y-27632 for 3h, as shown in (D). Scale bare = 50 µm (E).
814 Quantification of junctional β-catenin is reported for the different treatment across N=4
815 independent biological repeats (representing n=25 technical repeats). Violin plots representing
816 median and quartiles. One-Way ANOVA with Dunnett's multiple comparison post-test was
817 performed on biological repeats (F).
818
819 Figure 6: Reduced cell contractility promotes β-catenin nuclear activity and enhances binding to
820 mesodermal gene
821 (A) Representative immunoblot as explained in Supplementary Figure 6A. MYPT1^{CA}-NES-mNG
822 hiPSCs were induced with CHIR for 24hrs in the presence or absence of Doxycycline. Whole cell
823 lysate (WCL) was collected and loaded as input while cytosolic and nuclear fractions were
824 extracted. Fraction purity was probed using cytosolic (GAPDH) and nuclear (Lamin A/C) markers.
825 Active β-catenin (non-phospho S45) enrichment was probed for each fraction and α-Tubulin was
826 used as loading control. Molecular weights (M.W.) are displayed on the right side.
827 (B) Quantification of active β-catenin enrichment in the cytosolic (left) and nuclear (right)
828 fractions. N=4 independent biological repeats. Mean and S.D. are displayed. One-way ANOVA
829 with Šidák's multiple comparisons post-test was performed.

830 (C) Representative immunofluorescence for active non-phospho S45 β-catenin (Inverted LUT –
831 confocal slice) and mNeonGreen (MaxIP). MYPT1^{CA}-NES-mNG hiPSCs were fixed at 0h and 24h
832 post CHIR treatment +/- Doxycycline. Scale bar = 50 µm. Insets represent a magnified view of
833 the active non-phospho S45 β-catenin with an example of the nuclei binary mask overlaid
834 (pink). Scale bar = 10 µm.
835 (D, E) Stills confocal timelapse imaging of mEGFP-β-catenin knock-in hiPSCs treated with CHIR
836 +/- Y-26732 (Related to Supplementary movie 3). Time is shown in hours. Scale bar = 10 µm (D).
837 mEGFP-β-catenin intensity is reported as a scan line plot across a cell at 0h and 20h (E).
838 (F) Experiment design for GFP-Trap immunoprecipitation. mEGFP-β-catenin knock-in hiPSCs
839 were pre-treated with Vehicle or Y-27632 and differentiated for 24h. Nuclei were isolated and
840 nuclear lysates were mixed with GFP-Trap beads.
841 (G, H) Representative GFP-Trap immunoprecipitation of mEGFP-β-catenin knock-in hiPSCs,
842 probed for TCF7L2/TCF4 and α-Tubulin as loading control. Molecular weights (M.W.) are
843 displayed on the right side (G). Quantification of TCF4 (Prey) binding to mEGFP-β-catenin (Bait)
844 was measured by densitometry across N=3 independent biological repeats. Mean and S.D. are
845 displayed. One-way ANOVA with Šidák's multiple comparisons post-test was performed.
846 (I) CUT & RUN assay for IgG or β-catenin binding to *TBXT* promoter in WT hiPSC pre-treated with
847 Veh or Y-27632 (0h CHIR) or following 24h of CHIR treatment in the presence of absence of
848 ROCK inhibitor. N=3 independent biological repeats. Mean and S.D. are displayed. One-way
849 ANOVA with Šidák's multiple comparisons post-test was performed.
850
851 <u>Figure 7: Working model</u>
852 Effect of actomyosin contractility on mesoderm lineage commitment. Each panel represents a
853 specific contractile status at basal state (0h - top) and after 48h (bottom) of CHIR treatment. At
854 basal state, β-catenin is degraded and localized at AJs. The amount of junctional β-catenin
855 correlates with the level of contractility experienced by hiPSCs. During differentiation, β-catenin
856 accumulates in the nucleus and activates a mesoderm program through its binding with TCF4.
857
858 <u>Supplementary Figure 1: Increased actomyosin contractility is sufficient to block mesoderm</u>
859 <u>commitment and EMT (Related to Figure 1)</u>

860 (A) Experimental design. hiPSCs were pre-treated with 4 µg/mL CN03 or vehicle for 3 hours.
861 Differentiation was initiated with CHIR supplemented with Vehicle or 4 µg/mL CN03 for 24h
862 before fixation and staining.
863 (B) Representative MaxIP immunofluorescence of hiPSC treated as explained in (A) and stained
864 for phospho-MLC2 (Inverted LUT). Scale bar = 50 µm
865 (C, D) Representative MaxIP immunofluorescence of hiPSC treated as explained in (A) and
866 stained for Brachyury (Inverted LUT), nuclei and ZO-1. Scale bar = 50 µm (C). Violin plot (median,
867 quartiles) reporting the percentage of Brachyury-positive nuclei after 24h of differentiation and
868 quantified across N=4 independent biological repeats (representing n=20 technical repeats).
869 Unpaired t test was performed on biological replicates (D).
870 (E) Representative MaxIP immunofluorescence of Doxycycline-induced ROCK2^{CA} hiPSCs
871 (mVenus-positive) mixed with WT hiPSCs (mVenus-negative). Cells were stained for DNA
872 (Nuclei), F-actin (top – Inverted LUT) and phospho T18/S19 Myosin Light Chain 2 (Bottom -
873 ppMLC2 – Inverted LUT). Scale bar = 50 µm. Magnified views comparing mVenus-positive
874 (Green dotted ROI) and mVenus-negative (Black dotted ROI) areas are shown for F-Actin and
875 ppMLC2. Scale bar = 10 µm.
876 (F) Percentage of the ROI area positive for mVenus based on cluster considered as mVenus-
877 Negative and Positive using the ROCK2^{CA} line. On average, mVenus negative clusters have <15%
878 of their area positive for mVenus. Mean and S.E.M are displayed. n=7 (no Dox) and n=15 fields
879 of view (+Dox) across N=3 independent biological experiments.
880 (G) Representative MaxIP immunofluorescence of Doxycycline-induced MLCK^{CA} hiPSCs (mVenus-
881 positive) mixed with WT hiPSCs (mVenus-negative). Cells were stained for DNA (Nuclei), F-actin
882 (top – Inverted LUT) and phospho T18/S19 Myosin Light Chain 2 (Bottom - ppMLC2 – Inverted
883 LUT). Scale bar = 50 µm. Magnified views comparing mVenus-positive (Green dotted ROI) and
884 mVenus-negative (Black dotted ROI) areas are shown for F-Actin and ppMLC2. Scale bar = 10
885 µm.
886 (H) Percentage of the ROI area positive for mVenus based on cluster considered as mVenus-
887 Negative and Positive using the MLCK^{CA} line. On average, mVenus negative clusters have <15%
888 of their area positive for mVenus. Mean and S.E.M are displayed. n=7 (no Dox) and n=18 fields
889 of view (+Dox) across N=3 independent biological experiments.

890 (I, J) Representative MaxIP immunofluorescence for Brachyury in Vehicle (+Veh) and
891 Doxycycline-induced MLCK^{CA} co-culture. mVenus-positive cell clusters are highlighted by an
892 orange dotted line. Individual channels are inverted LUT. Scale bar = 50 µm (I). Percentage of
893 Brachyury-positive nuclei is reported as violin plot, comparing mVenus-positive *vs* mVenus-
894 negative cluster in the presence or absence of Doxycycline. Median (Plain red line) and quartiles
895 (Dotted black lines). n=7 (+Veh) and n=18 (+ Dox) fields of view (small dots) across N=3
896 independent biological repeats (large dots). One-way ANOVA with Tukey's multiple comparisons
897 post-test was performed (J).
898 (K) Representative MaxIP immunofluorescence for EOMES, Slug and ZO-1 in Doxycycline-
899 induced MLCK^{CA} co-culture. mVenus-positive cell clusters are highlighted by an orange dotted
900 line. Individual channels are inverted LUT. Scale bar = 50 µm.
901
902 <u>Supplementary Figure 2: Pharmaceutical inhibition of actomyosin contractility promotes hiPSC</u>
903 <u>and hESC conversion to the mesoderm lineage (Related to Figure 3)</u>
904 (A, B) Representative MaxIP immunofluorescences of hiPSCs treated with a ROCK inhibitor (Y-
905 27632) or Vehicle (H_2O) and stained for nuclei marker (DNA) and phospho T18/S19 Myosin Light
906 Chain 2 (ppMLC2 – Inverted LUT). Scale bar = 50 µm. Magnified views of the yellow dotted ROI
907 are shown for ppMLC2. Scale bar = 20 µm (A). Fraction of the cellular area positive for ppMLC2
908 following Y-27632 treatment and reported as violin pots. Median (Plain red line) and quartiles
909 (Dotted black lines). n=30 technical repeats across N=3 independent biological repeats. Two-
910 tailed unpaired t test was performed on the biological repeat (B).
911 (C) Relative expression of genes not directly related to mesoderm commitment at 0h and 48h
912 post CHIR treatment in the presence (+Y-27) or absence (+Veh) of ROCK inhibitor. N=4
913 independent biological repeats. Mean and S.D. are displayed. Two-tailed unpaired t test was
914 performed.
915 (D) Representative MaxIP immunofluorescences of hiPSC treated 48h with CHIR in the presence
916 (+ Y-27632) or absence (+ Veh) of ROCK inhibitor. Cells were stained for nuclei marker (DNA),
917 EMT markers (ZO-1 and Slug – Inverted LUT). Scale bar = 50 µm.
918 (E, F) Representative MaxIP immunofluorescences of hiPSCs treated with a ROCK inhibitor (H-
919 1152) or Vehicle (H_2O) and stained for nuclei marker (DNA) and phospho T18/S19 Myosin Light
920 Chain 2 (ppMLC2 – Inverted LUT). Scale bar = 50 µm. Magnified views of the yellow dotted ROI

921 are shown for ppMLC2. Scale bar = 20 µm (E). Fraction of the cellular area positive for ppMLC2
922 following H-1152 treatment and reported as violin pots. Median (Plain red line) and quartiles
923 (Dotted black lines). n=15 technical repeats across N=3 independent biological repeats. Two-
924 tailed unpaired t test was performed on the biological repeats (F).
925 (G-K) Relative expression of mesoderm markers (*TBXT*, *MESP1, TBX6*) (G-I) and EMT markers
926 (*SNAI1, SNAI2*) (J, K) 48h post CHIR treatment in the presence (+H-1152) or absence (+Veh) of
927 ROCK inhibitor. N=3 independent biological repeats. Mean and S.D. are displayed. Two-tailed
928 unpaired t test was performed.
929 (L) Immunoblot probing for mesoderm marker expression (T/Bra) and cell death marker (PARP
930 cleavage) during hiPSC-to-mesoderm commitment (0h-48h CHIR) in the presence of ROCK
931 inhibitor (+H-1152). Addition of the pan-caspase inhibitor Q-VD-OPH (+ Q-VD) to the
932 differentiation medium totally blocks mesoderm commitment and was used as control. α-
933 Tubulin was used as loading control. Molecular weights (M.W.) are displayed on the right side.
934 (M) Representative MaxIP immunofluorescences for mesoderm marker Brachyury (T/Bra –
935 Inverted LUT) and nuclei. Cells were fixed 24h post-CHIR treatment in the presence or absence
936 of ROCK inhibitor H-1152. Scale bar = 50 µm
937 (N) Representative immunoblot of PARP (cell death), T/Bra (mesoderm), Oct4 and Nanog
938 (Pluripotency markers) using hESC H9 in the presence (+ Y-27632) or absence (+ Veh) of ROCK
939 inhibitor, as shown in Figure 3A. Molecular weights (M.W.) are displayed on the right side.
940 (O-Q) Brachyury expression (O), PARP cleavage (P) and Nanog expression (Q) was quantified by
941 densitometry and normalized to α-Tubulin as loading control across N=4 (PARP) and N=3
942 (Brachyury and Nanog) independent biological repeats. Mean and S.D. are displayed. Two-tailed
943 unpaired t test was performed.
944
945 <u>Supplementary Figure 3: hiPSC differentiation along the cardiac mesoderm increases</u>
946 <u>actomyosin-driven contractility</u>
947 (A) Bright field imaging of WT hiPSCs treated with CHIR in the presence or absence of a pan-
948 Caspase inhibitor Q-VD-OPH. Retraction area is highlighted in yellow. Time is presented as
949 hh:mm. Scale bar = 20 µm. (Related to Supplementary movie 1).

950 (B, C) Confocal XZ orthogonal views (B) and Maximum Intensity Projections (MaxIP) (C) of hiPSCs
951 at basal state (0h CHIR) or post-CHIR treatment (24h and 48h CHIR), stained for DNA (Cyan) and
952 F-Actin (Grey). Scale bar = 10 µm.
953 (D) Quantification of the monolayer height at 0h, 24h and 48h post CHIR treatment from (B).
954 Violin plots represent individual measurements (small dots) averaged for each biological repeat
955 (large dots). Median (Plain red line) and quartiles (Dotted black lines). n=32 technical repeats
956 across N=7 independent biological repeats. A Kruskal-Wallis test with Dunn's multiple
957 comparison post-test was performed on biological repeats.
958 (E-G) Representative MaxIP immunofluorescence of WT hiPSC during CHIR treatment. Fixed cells
959 were stained for DNA marker (Hoechst). Scale bar = 20 µm (E). Average nuclear size from n=15
960 fields of view across N=3 independent biological repeats. Median (Plain red line) and quartiles
961 (Dotted black lines) are displayed. Two-tailed unpaired t test was performed (F). Correlation of
962 nuclear area over cell number for each field of view during CHIR treatment. Biological repeats
963 are color-coded. Pearson correlation coefficient is displayed for each treatment (G).
964 (H) Representative MaxIP immunofluorescence of hiPSCs at basal state (0h) or post-CHIR
965 treatment (24 and 48h) stained for phospho T18/S19 MLC2 (ppMLC2). Pixels are color-coded by
966 intensity using the fire LUT. Scale bar = 50 µm
967 (I) Percentage of ppMLC2-positive area at 0hr, 24hrs, 48hrs post CHIR is reported as violin plots.
968 Median (Plain red line) and quartiles (Dotted black lines). n=15 technical repeats across N=3
969 independent biological repeats. A Kruskal-Wallis test with Dunn's multiple comparison post-test
970 was performed on the technical repeats.
971 (J) Retardance measurements obtained from hiPSCs at basal state (0h), post-CHIR treatment
972 (24h, 48h, 72h) or treated with Y-27632 at 0h (Y-27) using Quantitative Polarization Microscopy
973 imaging. Median (Plain red line) and quartiles (Dotted black lines). n=240 technical repeats for
974 0hr, 24hrs, 48hrs, 72hrs and n=120 technical repeats for Y-27 across N=3 independent biological
975 repeats. A one-way ANOVA with Šidák's multiple comparisons post-test was performed on the
976 biological repeats.
977
978 <u>Supplementary Figure 4: Key mechanosensitive pathways are not involved in mesoderm</u>
979 <u>specification enhancement following decreased contractility</u>

980 (A, B) Immunoblot for phospho S127 YAP (pYAP) and total YAP following differentiation (0-48h
981 CHIR) in the presence or absence of ROCK inhibitor Y-27632. Brachyury expression was also
982 probed as an internal positive control and α-Tubulin was used as loading control. Molecular
983 weights (M.W.) are displayed on the right side (A). Ratio of phospho/total YAP was quantified
984 across N=4 independent biological repeats. Mean and S.D. are displayed. One-way ANOVA with
985 Šidák's multiple comparisons post-test was performed (B)
986 (C) Relative expression of YAP-target genes *CTGF* and *CYR61* during differentiation +/- Y-27632.
987 N=4 independent biological repeats. Mean and S.D. are displayed. One-way ANOVA with Šidák's
988 multiple comparisons post-test was performed.
989 (D) Relative expression of canonical WNT (*WNT3A, WNT8A*), non-canonical WNT (*WNT4*) and
990 mesoderm marker (*TBX6*) in MYPT1^{CA}-NES-mNG cells treated with CHIR (0-48h) in the presence
991 of Vehicle or Doxycycline. N=3 independent biological repeats. Mean and S.D. are displayed.
992 One-way ANOVA with Šidák's multiple comparisons post-test was performed.
993 (E) Relative expression of *TBX6* and *MESP1* (mesoderm markers) following CHIR treatment +/- Y-
994 27632 complemented or not with 7.5 µM Porcupine inhibitor (IWP-2 or DMSO respectively).
995 N=3 independent biological repeats. Mean and S.D. are displayed. One-way ANOVA with Tukey's
996 multiple comparisons post-test was performed.
997
998 <u>Supplementary Figure 5: EGTA treatment and validation *CTNNA1* knockdown hiPSCs (related to</u>
999 <u>Figure 4)</u>
1000 (A) Bright field picture showing the colony morphology following EGTA pre-treatment. Colony
1001 appears less compact and individual cell boundaries can be distinguished. Scale bar = 20 µm.
1002 (B, C) Representative immunofluorescence of hiPSCs treated as shown in Figure 4A and stained
1003 for Brachyury. Scale bar = 50 µm (B). Quantification of Brachyury-positive nuclei is shown
1004 following EGTA treatment. Mean and S.D. are displayed. n=18 (Veh) and n=20 fields of view
1005 across N=3 independent biological repeats. Two-tailed unpaired t test was performed on
1006 biological repeats (C).
1007 (D, E) Representative immunofluorescence of hiPSC treated as shown in Figure 4A and stained
1008 for ppMLC2. Scale bar = 50 µm (D). Quantification of ppMLC2-positive area is shown following
1009 EGTA treatment. Mean and S.D. are displayed. n=20 (Veh) and n=25 fields of view across N=4

1010 independent biological repeats. Two-tailed unpaired t test was performed on biological repeats
1011 (E).
1012 (F-I) Representative immunoblot of control (Ctr) or *CTNNA1* knockdown hiPSCs, probed for α-
1013 catenin, Nanog and Oct-4 (pluripotency) and α-Tubulin as loading control. Molecular weights
1014 (M.W.) are displayed on the right side (F). Quantification of α-catenin (G), Nanog (H) and Oct-4
1015 (I) expression was obtained by densitometry across N=5-6 (α-catenin), N=4 (Nanog) and N=3
1016 (Oct-4) independent biological repeats. Mean and S.D. are displayed. One-Way ANOVA with
1017 Dunnett's multiple comparisons post-test was performed.
1018
1019 <u>Supplementary Figure 6: Contractility affects β-catenin localization at adherens junctions</u>
1020 <u>(related to Figure 5)</u>
1021 (A) Immunoblot assessing the effects of CN03 treatment at 4h and 16h. Membrane was probed
1022 for total and phospho-ML2 (MLC2 and ppMLC2 respectively), Nanog and Oct-4 and α-Tubulin as
1023 loading control. Molecular weights (M.W.) are displayed on the right side.
1024 (B) Independent technical repeats from Figure 5 A-B. Repeats across the 3 biological repeats
1025 were averaged and shown as a dot with error bars (S.D.).
1026 (C) Still picture from overnight confocal imaging of mEGFP-β-catenin knock-in hiPSC treated with
1027 Vehicle, CN03 and Y-27632 at basal state. Pixels are color-coded by intensity using the Red Fire
1028 LUT. Scale bar = 20 µm. (Related to Supplementary video 2).
1029 (D) Experimental design. Cells were pre-treated overnight with Vehicle or Y-27632 or CN03 in
1030 mTeSR1 and differentiated using CHIR media complemented with Vehicle or Y-27632 or CN03
1031 for 24h before collecting protein lysates
1032 (E, F) Representative immunoblot for total β-catenin. Membrane was also probed for Brachyury
1033 to show effect of each drug and α-Tubulin as loading control. Molecular weights (M.W.) are
1034 displayed on the right side (E). β-catenin expression was quantified across N=6 (Vehicle and Y-
1035 27632) and N=4 (CN03) independent biological repeats. Mean and S.D. are displayed. One-way
1036 ANOVA with Šidák's multiple comparisons post-test was performed (F).
1037
1038 <u>Supplementary Figure 7: Reduced cell contractility promotes nuclear accumulation of β-catenin</u>
1039 <u>(related to Figure 6)</u>
1040 (A) Experiment design for treatments and cell fractionation.

1041 (B) Compartment purity following fractionation was assessed by quantifying Lamin A/C and
1042 GAPDH enrichment in both, cytosolic and nuclear fractions across N=4 independent biological
1043 repeats.
1044 (C) Schematic representation of the quantification pipeline for nuclear β-catenin.
1045 (D) Quantification of active non-phospho S45 β-catenin mean intensity as depicted in (C). n =
1046 10-12 technical repeats across N=3 independent biological repeats. Mean and S.D. are
1047 displayed. One-way ANOVA with Šidák's multiple comparisons post-test was performed.
1048 (E) Expression of TCF genes (transcripts per million – tpm) from parental WTC hiPSC obtained
1049 from the Allen Institute transcriptomic data. N=6 independent biological repeats.
1050 (F) Positive control for CUT & RUN assay using IgG and β-catenin binding to WNT target genes
1051 (*AXIN2* and *SP5*) between 0h and 24h of CHIR treatment. Mean and S.D. are displayed. N=3
1052 independent biological repeats. One-Way ANOVA with Dunnett's multiple comparisons post-test
1053 was performed.
1054 (G) Relative expression of WNT target genes (*LEF1* and *AXIN2*) with increasing concentration of
1055 CHIR in the presence (Magenta) or absence (Cyan) of ROCK inhibitor Y-27632. N=7 independent
1056 biological repeats. Mean and S.E.M. are displayed. One-way ANOVA with Šidák's multiple
1057 comparisons post-test was performed.
1058
1059 <u>Supplementary Video 1</u>
1060 Bright field movie of hiPSC colony treated with CHIR supplemented with Vehicle (DMSO) or Q-
1061 VD-OPH (cell death inhibitor). Time in hh:mm. Scale bar = 20 μm.
1062
1063 <u>Supplementary Video 2</u>
1064 Confocal imaging of mEGFP-β-catenin knock-in hiPSC treated with Vehicle (water), 4μg/mL
1065 CN03 or 10 μM Y-27632 in mTeSR1. Red Fire LUT reflects the pixel intensity. Time in hh:mm:ss.
1066 Scale bar = 20 μm.
1067
1068 <u>Supplementary Video 3</u>
1069 Confocal imaging of mEGFP-β-catenin knock-in hiPSC treated with CHIR supplemented with
1070 Vehicle (water) or 10 μM Y-27632. Time in hh:mm. Scale bar = 10 μm.
1071

References

1. Firmin, J. *et al.* Mechanics of human embryo compaction. *Nature* **629**, 646–651 (2024).
2. Mundhe, G. *et al.* Spatial patterning of contractility by a mechanogen gradient underlies *Drosophila* gastrulation. Preprint at https://doi.org/10.1101/2025.04.11.648359 (2025).
3. Lecuit, T. & Lenne, P.-F. Cell surface mechanics and the control of cell shape, tissue patterns and morphogenesis. *Nat Rev Mol Cell Biol* **8**, 633–644 (2007).
4. Goodwin, K. & Nelson, C. M. Mechanics of Development. *Dev Cell* **56**, 240–250 (2021).
5. Caldarelli, P. *et al.* Self-organized tissue mechanics underlie embryonic regulation. *Nature* **633**, 887–894 (2024).
6. De Belly, H., Paluch, E. K. & Chalut, K. J. Interplay between mechanics and signalling in regulating cell fate. *Nat Rev Mol Cell Biol* **23**, 465–480 (2022).
7. Khalilgharibi, N. *et al.* Stress relaxation in epithelial monolayers is controlled by the actomyosin cortex. *Nat Phys* **15**, 839–847 (2019).
8. Yang, Y.-A. *et al.* Local contractions regulate E-cadherin rigidity sensing. *Sci Adv* **8**, (2022).
9. Shyer, A. E. *et al.* Emergent cellular self-organization and mechanosensation initiate follicle pattern in the avian skin. *Science (1979)* **357**, 811–815 (2017).
10. Behrndt, M. *et al.* Forces Driving Epithelial Spreading in Zebrafish Gastrulation. *Science (1979)* **338**, 257–260 (2012).
11. Hall, E. T., Hoesing, E., Sinkovics, E. & Verheyen, E. M. Actomyosin contractility modulates Wnt signaling through adherens junction stability. *Mol Biol Cell* **30**, 411–426 (2019).
12. Lian, X. *et al.* Robust cardiomyocyte differentiation from human pluripotent stem cells via temporal modulation of canonical Wnt signaling. *Proceedings of the National Academy of Sciences* **109**, (2012).
13. Lian, X. *et al.* Directed cardiomyocyte differentiation from human pluripotent stem cells by modulating Wnt/β-catenin signaling under fully defined conditions. *Nat Protoc* **8**, 162–175 (2013).
14. Zhao, M., Tang, Y., Zhou, Y. & Zhang, J. Deciphering Role of Wnt Signalling in Cardiac Mesoderm and Cardiomyocyte Differentiation from Human iPSCs: Four-dimensional control of Wnt pathway for hiPSC-CMs differentiation. *Sci Rep* **9**, 19389 (2019).
15. Fort, L., Gama, V. & Macara, I. G. Stem cell conversion to the cardiac lineage requires nucleotide signalling from apoptosing cells. *Nat Cell Biol* **24**, 434–447 (2022).
16. Muncie, J. M. *et al.* Mechanical Tension Promotes Formation of Gastrulation-like Nodes and Patterns Mesoderm Specification in Human Embryonic Stem Cells. *Dev Cell* **55**, 679-694.e11 (2020).
17. Przybyla, L., Lakins, J. N. & Weaver, V. M. Tissue Mechanics Orchestrate Wnt-Dependent Human Embryonic Stem Cell Differentiation. *Cell Stem Cell* **19**, 462–475 (2016).
18. van der Wal, T. & van Amerongen, R. Walking the tight wire between cell adhesion and WNT signalling: a balancing act for β-catenin. *Open Biol* **10**, (2020).

19. Orsulic, S., Huber, O., Aberle, H., Arnold, S. & Kemler, R. E-cadherin binding prevents β-catenin nuclear localization and β-catenin/LEF-1-mediated transactivation. *J Cell Sci* **112**, 1237–1245 (1999).
20. Pukhlyakova, E., Aman, A. J., Elsayad, K. & Technau, U. β-Catenin–dependent mechanotransduction dates back to the common ancestor of Cnidaria and Bilateria. *Proceedings of the National Academy of Sciences* **115**, 6231–6236 (2018).
21. Gayrard, C., Bernaudin, C., Déjardin, T., Seiler, C. & Borghi, N. Src- and confinement-dependent FAK activation causes E-cadherin relaxation and β-catenin activity. *Journal of Cell Biology* **217**, 1063–1077 (2018).
22. Schmidt, G. *et al.* Gln 63 of Rho is deamidated by Escherichia coli cytotoxic necrotizing factor-1. *Nature* **387**, 725–729 (1997).
23. Flatau, G. *et al.* Toxin-induced activation of the G protein p21 Rho by deamidation of glutamine. *Nature* **387**, 729–733 (1997).
24. Totsukawa, G. *et al.* Distinct roles of ROCK (Rho-kinase) and MLCK in spatial regulation of MLC phosphorylation for assembly of stress fibers and focal adhesions in 3T3 fibroblasts. *J Cell Biol* **150**, 797–806 (2000).
25. Shi, Y., Ohler, L. S., de Jesus, B. N. & Dickinson, D. J. Opposing actomyosin pools generate cortical flows that establish epithelial polarity. *Biorxiv* (2024).
26. Matsumura, F., Yamakita, Y. & Yamashiro, S. Myosin Phosphatase-targeting Subunit 1 Controls Chromatid Segregation. *Journal of Biological Chemistry* **286**, 10825–10833 (2011).
27. Kiss, A., Erdődi, F. & Lontay, B. Myosin phosphatase: Unexpected functions of a long-known enzyme. *Biochimica et Biophysica Acta (BBA) - Molecular Cell Research* **1866**, 2–15 (2019).
28. Yamamoto, K. *et al.* Optogenetic relaxation of actomyosin contractility uncovers mechanistic roles of cortical tension during cytokinesis. *Nat Commun* **12**, 7145 (2021).
29. Makishima, M. *et al.* Induction of differentiation of human leukemia cells by inhibitors of myosin light chain kinase. *FEBS Lett* **287**, 175–177 (1991).
30. Hookway, C. *et al.* A human induced pluripotent stem (hiPS) cell model for the holistic study of epithelial to mesenchymal transitions (EMTs). *BioRxiv* (2024).
31. Lomakin, A. J. *et al.* The nucleus acts as a ruler tailoring cell responses to spatial constraints. *Science (1979)* **370**, (2020).
32. de Leeuw, N. F., Budhathoki, R., Russell, L. J., Loerke, D. & Blankenship, J. T. Nuclei as mechanical bumpers during epithelial remodeling. *Journal of Cell Biology* **223**, (2024).
33. Wang, W., Miller, J. P., Pannullo, S. C., Reinhart-King, C. A. & Bordeleau, F. Quantitative assessment of cell contractility using polarized light microscopy. *J Biophotonics* **11**, (2018).
34. Stronati, E. *et al.* YAP1 regulates the self-organized fate patterning of hESC-derived gastruloids. *Stem Cell Reports* **17**, 211–220 (2022).
35. Pagliari, S. *et al.* YAP–TEAD1 control of cytoskeleton dynamics and intracellular tension guides human pluripotent stem cell mesoderm specification. *Cell Death Differ* **28**, 1193–1207 (2021).
36. Meyer, K., Lammers, N. C., Bugaj, L. J., Garcia, H. G. & Weiner, O. D. Optogenetic control of YAP reveals a dynamic communication code for stem cell fate and proliferation. *Nat Commun* **14**, 6929 (2023).

37. Pinheiro, D. & Bellaïche, Y. Mechanical Force-Driven Adherens Junction Remodeling and Epithelial Dynamics. *Dev Cell* **47**, 3–19 (2018).
38. Koch, A. W., Pokutta, S., Lustig, A. & Engel, J. Calcium Binding and Homoassociation of E-cadherin Domains. *Biochemistry* **36**, 7697–7705 (1997).
39. Smutny, M. *et al.* Myosin II isoforms identify distinct functional modules that support integrity of the epithelial zonula adherens. *Nat Cell Biol* **12**, 696–702 (2010).
40. le Duc, Q. *et al.* Vinculin potentiates E-cadherin mechanosensing and is recruited to actin-anchored sites within adherens junctions in a myosin II–dependent manner. *Journal of Cell Biology* **189**, 1107–1115 (2010).
41. Bedzhov, I. *et al.* Adhesion, but not a specific cadherin code, is indispensable for ES cell and induced pluripotency. *Stem Cell Res* **11**, 1250–1263 (2013).
42. Röper, J.-C. *et al.* The major β-catenin/E-cadherin junctional binding site is a primary molecular mechano-transductor of differentiation in vivo. *Elife* **7**, (2018).
43. Funa, N. S. *et al.* β-Catenin Regulates Primitive Streak Induction through Collaborative Interactions with SMAD2/SMAD3 and OCT4. *Cell Stem Cell* **16**, 639–652 (2015).
44. Zimmerli, D. *et al.* TBX3 acts as tissue-specific component of the Wnt/β-catenin transcriptional complex. *Elife* **9**, (2020).
45. Mukherjee, S., Luedeke, D. M., McCoy, L., Iwafuchi, M. & Zorn, A. M. SOX transcription factors direct TCF-independent WNT/β-catenin responsive transcription to govern cell fate in human pluripotent stem cells. *Cell Rep* **40**, 111247 (2022).
46. Moreira, S. *et al.* A Single TCF Transcription Factor, Regardless of Its Activation Capacity, Is Sufficient for Effective Trilineage Differentiation of ESCs. *Cell Rep* **20**, 2424–2438 (2017).
47. Cadigan, K. M. & Waterman, M. L. TCF/LEFs and Wnt Signaling in the Nucleus. *Cold Spring Harb Perspect Biol* **4**, a007906–a007906 (2012).
48. Gerner-Mauro, K. N., Akiyama, H. & Chen, J. Redundant and additive functions of the four Lef/Tcf transcription factors in lung epithelial progenitors. *Proceedings of the National Academy of Sciences* **117**, 12182–12191 (2020).
49. Guo, Q. *et al.* A β-catenin-driven switch in TCF/LEF transcription factor binding to DNA target sites promotes commitment of mammalian nephron progenitor cells. *Elife* **10**, (2021).
50. Blassberg, R. *et al.* Sox2 levels regulate the chromatin occupancy of WNT mediators in epiblast progenitors responsible for vertebrate body formation. *Nat Cell Biol* **24**, 633–644 (2022).
51. Yi, F., Pereira, L. & Merrill, B. J. Tcf3 Functions as a Steady-State Limiter of Transcriptional Programs of Mouse Embryonic Stem Cell Self-Renewal. *Stem Cells* **26**, 1951–1960 (2008).
52. Pereira, L., Yi, F. & Merrill, B. J. Repression of Nanog Gene Transcription by Tcf3 Limits Embryonic Stem Cell Self-Renewal. *Mol Cell Biol* **26**, 7479–7491 (2006).
53. Wray, J. *et al.* Inhibition of glycogen synthase kinase-3 alleviates Tcf3 repression of the pluripotency network and increases embryonic stem cell resistance to differentiation. *Nat Cell Biol* **13**, 838–845 (2011).
54. Cole, M. F., Johnstone, S. E., Newman, J. J., Kagey, M. H. & Young, R. A. Tcf3 is an integral component of the core regulatory circuitry of embryonic stem cells. *Genes Dev* **22**, 746–755 (2008).

1211 55. Brunet, T. *et al.* Evolutionary conservation of early mesoderm specification by
1212 mechanotransduction in Bilateria. *Nat Commun* **4**, 2821 (2013).
1213 56. Vasic, I. *et al.* Loss of TJP1 disrupts gastrulation patterning and increases
1214 differentiation toward the germ cell lineage in human pluripotent stem cells. *Dev Cell*
1215 **58**, 1477-1488.e5 (2023).
1216 57. Maytum, A. *et al.* Chromatin priming elements direct tissue-specific gene activity
1217 before hematopoietic specification. *Life Sci Alliance* **7**, e202302363 (2024).
1218 58. Le, H. Q. *et al.* Mechanical regulation of transcription controls Polycomb-mediated
1219 gene silencing during lineage commitment. *Nat Cell Biol* **18**, 864–875 (2016).
1220 59. Roura, S., Miravet, S., Piedra, J., de Herreros, A. G. & Duñach, M. Regulation of E-
1221 cadherin/Catenin Association by Tyrosine Phosphorylation. *Journal of Biological*
1222 *Chemistry* **274**, 36734–36740 (1999).
1223 60. Kashkooli, L., Rozema, D., Espejo-Ramirez, L., Lasko, P. & Fagotto, F. Ectoderm to
1224 mesoderm transition by down-regulation of actomyosin contractility. *PLoS Biol* **19**,
1225 e3001060 (2021).
1226

Figure 1

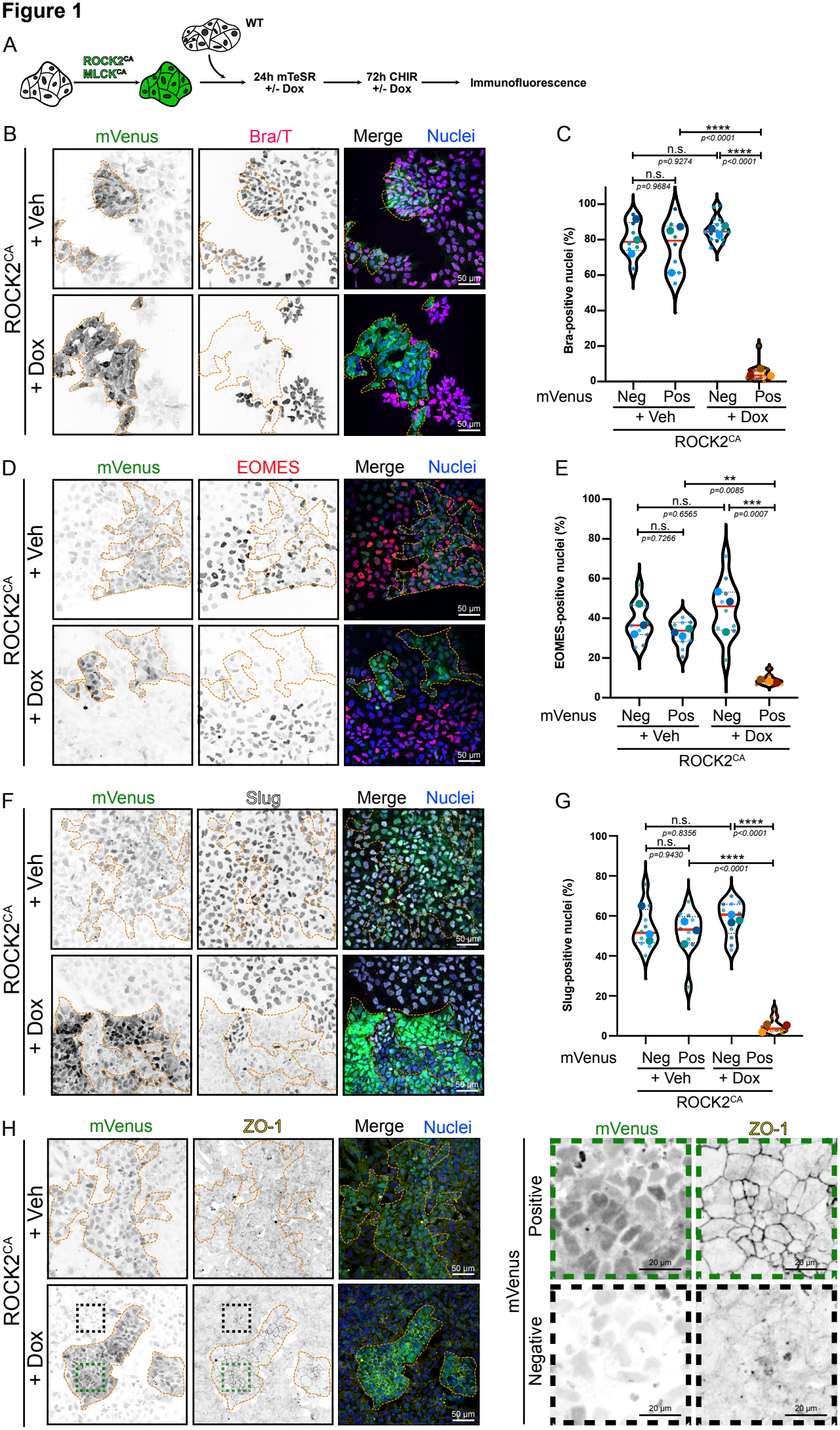
A
WT
ROCK2CA
MLCKCA
24h mTeSR
+/- Dox
72h CHIR
+/- Dox
Immunofluorescence
B
mVenus
Bra/T
Merge
Nuclei
ROCK2CA
+ Veh
+ Dox
50 µm
C
Bra-positive nuclei (%)
n.s.
p=0.9684
n.s.
p=0.9274
****
p<0.0001
****
p<0.0001
mVenus
Neg
Pos
Neg
Pos
+ Veh
+ Dox
ROCK2CA
D
mVenus
EOMES
Merge
Nuclei
ROCK2CA
+ Veh
+ Dox
50 µm
E
EOMES-positive nuclei (%)
n.s.
p=0.7266
n.s.
p=0.6565
**
p=0.0085
***
p=0.0007
mVenus
Neg
Pos
Neg
Pos
+ Veh
+ Dox
ROCK2CA
F
mVenus
Slug
Merge
Nuclei
ROCK2CA
+ Veh
+ Dox
50 µm
G
Slug-positive nuclei (%)
n.s.
p=0.9430
n.s.
p=0.8356
****
p<0.0001
****
p<0.0001
mVenus
Neg
Pos
Neg
Pos
+ Veh
+ Dox
ROCK2CA
H
mVenus
ZO-1
Merge
Nuclei
ROCK2CA
+ Veh
+ Dox
50 µm
mVenus
ZO-1
mVenus
Positive
Negative
20 µm

Figure 2

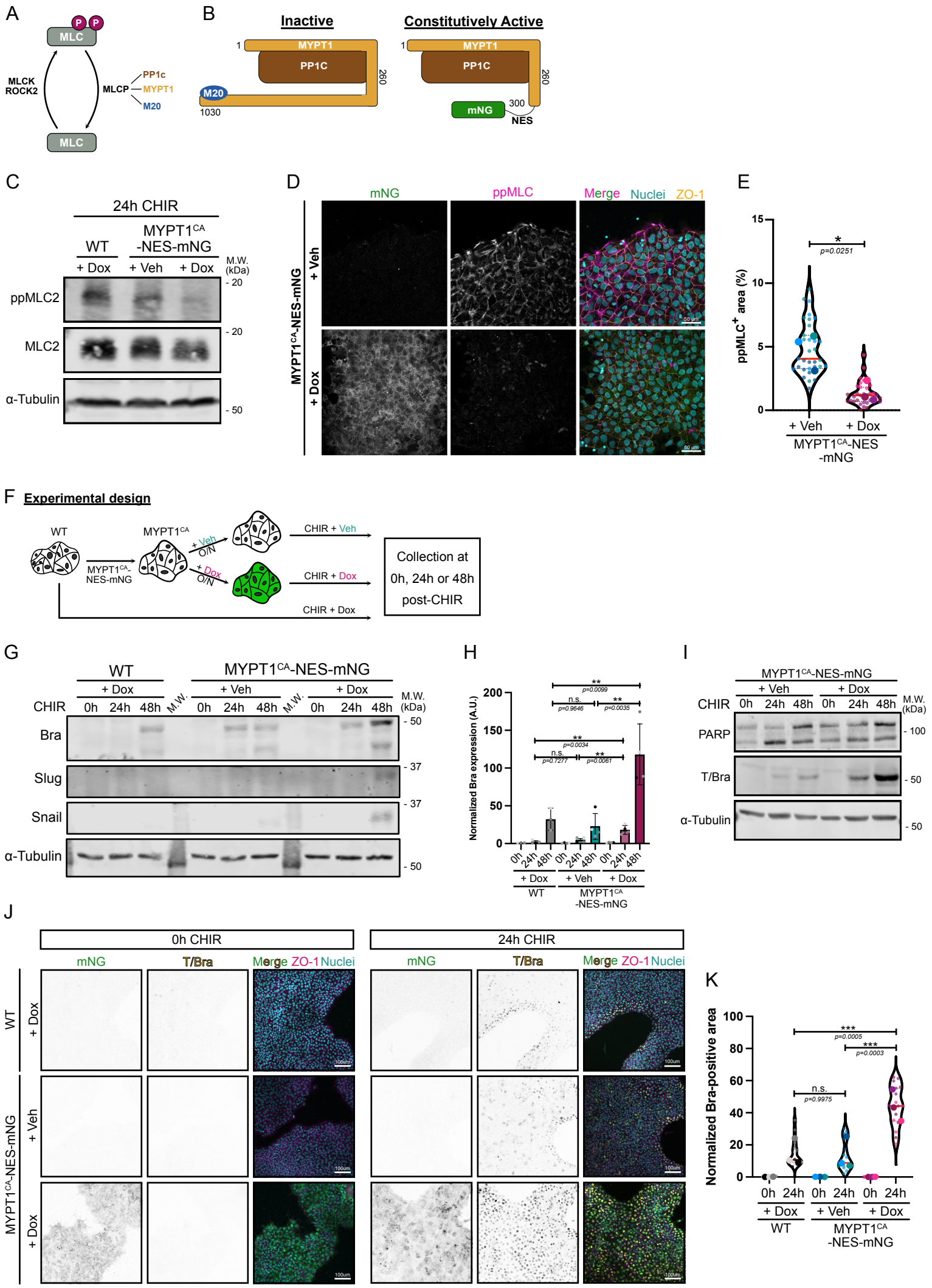
A
MLC
P P
MLCK
ROCK2
MLCP
PP1c
MYPT1
M20
MLC
B
Inactive
Constitutively Active
MYPT1
PP1C
M20
1
1030
260
mNG
300
NES
C
24h CHIR
WT
MYPT1CA -NES-mNG
+ Dox
+ Veh
+ Dox
M.W. (kDa)
ppMLC2
MLC2
α-Tubulin
- 20
- 20
- 50
D
mNG
ppMLC
Merge
Nuclei
ZO-1
MYPT1CA-NES-mNG
+ Veh
+ Dox
E
ppMLC+ area (%)
15
10
5
0
*
p=0.0251
+ Veh
+ Dox
MYPT1CA-NES -mNG
F
Experimental design
WT
MYPT1CA
MYPT1CA-NES-mNG
+ Veh O/N
+ Dox O/N
CHIR + Veh
CHIR + Dox
CHIR + Dox
Collection at 0h, 24h or 48h post-CHIR
G
WT
MYPT1CA-NES-mNG
+ Dox
+ Veh
+ Dox
CHIR
0h 24h 48h M.W. 0h 24h 48h M.W. 0h 24h 48h
M.W. (kDa)
Bra
Slug
Snail
α-Tubulin
- 50
- 37
- 37
- 50
H
Normalized Bra expression (A.U.)
200
150
100
50
0
**
p=0.0099
n.s.
p=0.9646
**
p=0.0035
**
p=0.0034
n.s.
p=0.7277
**
p=0.0061
0h 24h 48h 0h 24h 48h 0h 24h 48h
+ Dox
+ Veh
+ Dox
WT
MYPT1CA -NES-mNG
I
MYPT1CA-NES-mNG
+ Veh
+ Dox
CHIR
0h 24h 48h 0h 24h 48h
M.W. (kDa)
PARP
T/Bra
α-Tubulin
- 100
- 50
- 50
J
0h CHIR
24h CHIR
mNG
T/Bra
Merge ZO-1 Nuclei
WT
+ Dox
MYPT1CA-NES-mNG
+ Veh
+ Dox
K
Normalized Bra-positive area
100
80
60
40
20
0
***
p=0.0005
***
p=0.0003
n.s.
p=0.9975
0h 24h 0h 24h 0h 24h
+ Dox
+ Veh
+ Dox
WT
MYPT1CA -NES-mNG

Figure 3

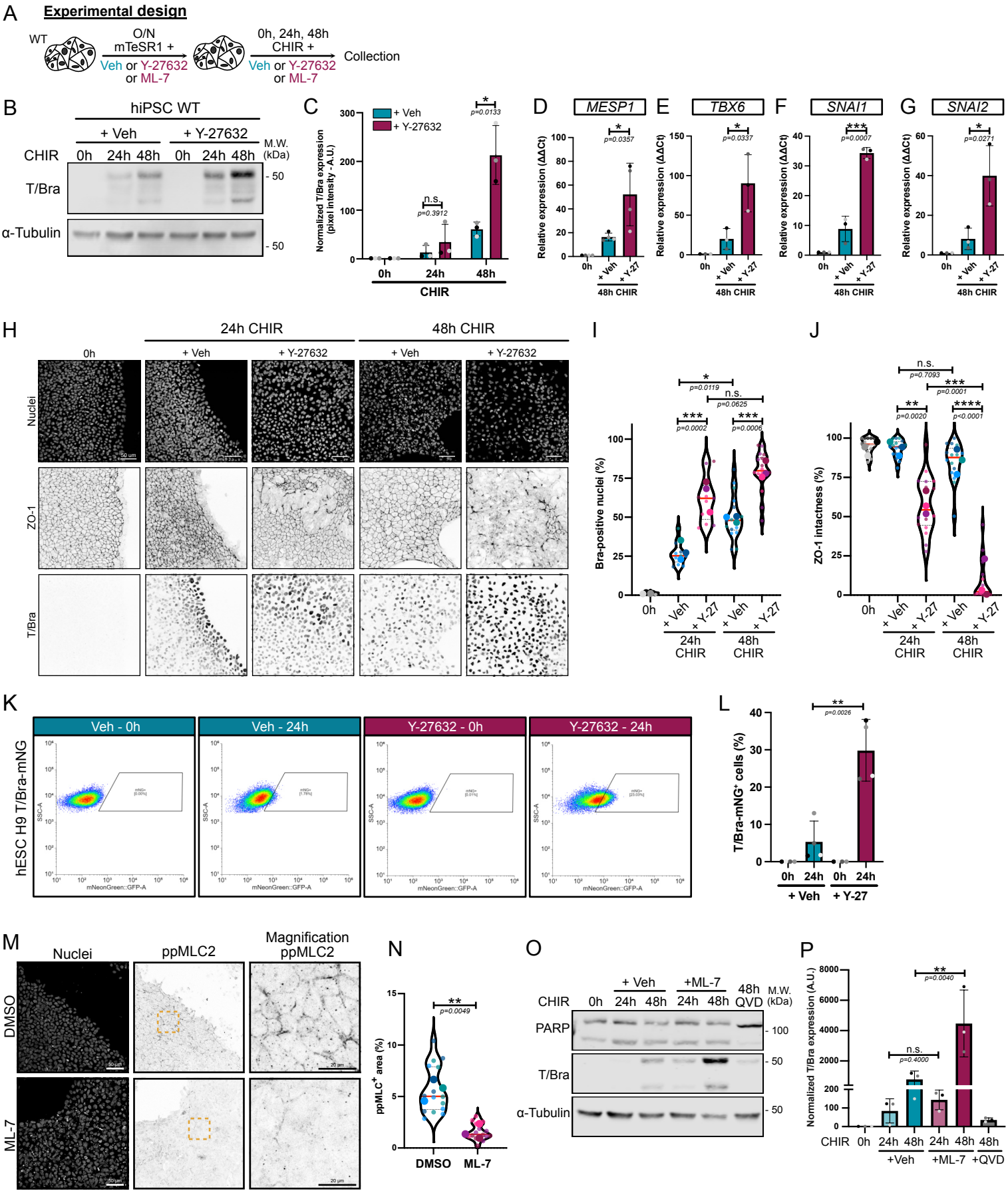
A
Experimental design
WT
O/N
mTeSR1 +
Veh or Y-27632
or ML-7
0h, 24h, 48h
CHIR +
Veh or Y-27632
or ML-7
Collection
B
hiPSC WT
+ Veh
+ Y-27632
CHIR
0h 24h 48h 0h 24h 48h
M.W. (kDa)
T/Bra
α-Tubulin
- 50
- 50
C
+ Veh
+ Y-27632
Normalized T/Bra expression (pixel intensity - A.U.)
n.s.
p=0.3912
*
p=0.0133
0h
24h
48h
CHIR
D
MESP1
*
p=0.0357
E
TBX6
*
p=0.0337
F
SNAI1
***
p=0.0007
G
SNAI2
*
p=0.0271
Relative expression (ΔΔCt)
0h
+ Veh
+ Y-27
48h CHIR
H
24h CHIR
48h CHIR
0h
+ Veh
+ Y-27632
+ Veh
+ Y-27632
Nuclei
ZO-1
T/Bra
I
Bra-positive nuclei (%)
*
p=0.0119
n.s.
p=0.0625
***
p=0.0002
***
p=0.0006
0h
+ Veh
+ Y-27
24h CHIR
48h CHIR
J
ZO-1 intactness (%)
n.s.
p=0.7093
***
p=0.0001
**
p=0.0020
****
p<0.0001
K
hESC H9 T/Bra-mNG
Veh - 0h
Veh - 24h
Y-27632 - 0h
Y-27632 - 24h
mNeonGreen::GFP-A
SSC-A
L
T/Bra-mNG+ cells (%)
**
p=0.0026
0h 24h 0h 24h
+ Veh
+ Y-27
M
Nuclei
ppMLC2
Magnification ppMLC2
DMSO
ML-7
N
ppMLC+ area (%)
**
p=0.0049
DMSO
ML-7
O
CHIR
0h 24h 48h 24h 48h 48h
+ Veh
+ ML-7
QVD
M.W. (kDa)
PARP
T/Bra
α-Tubulin
- 100
- 50
- 50
P
Normalized T/Bra expression (A.U.)
**
p=0.0040
n.s.
p=0.4000
CHIR 0h 24h 48h 24h 48h 48h
+Veh
+ML-7
+QVD
Q
Experimental design
CHIR
Pre-treatment
Differentiation
-12h
Veh or Y-27
+ Veh or Y-27
0h
No pre-treatment
+ Veh or Y-27
+12h
No pre-treatment
+ Veh or Y-27
- 12h
0h
+ 12h
+ 24h
R
24h CHIR + Veh
24h CHIR + Y-27632
0h CHIR
- 12h
0h
+12h
M.W.
T/Bra
α-Tubulin
- 50
- 50
S
+ Veh
+ Y-27632
Normalized Bra/Tubulin
****
p<0.0001
*
p=0.0164
n.s.
p=0.7735
0h CHIR
-12h
0h
+12h
24h CHIR

Figure 4

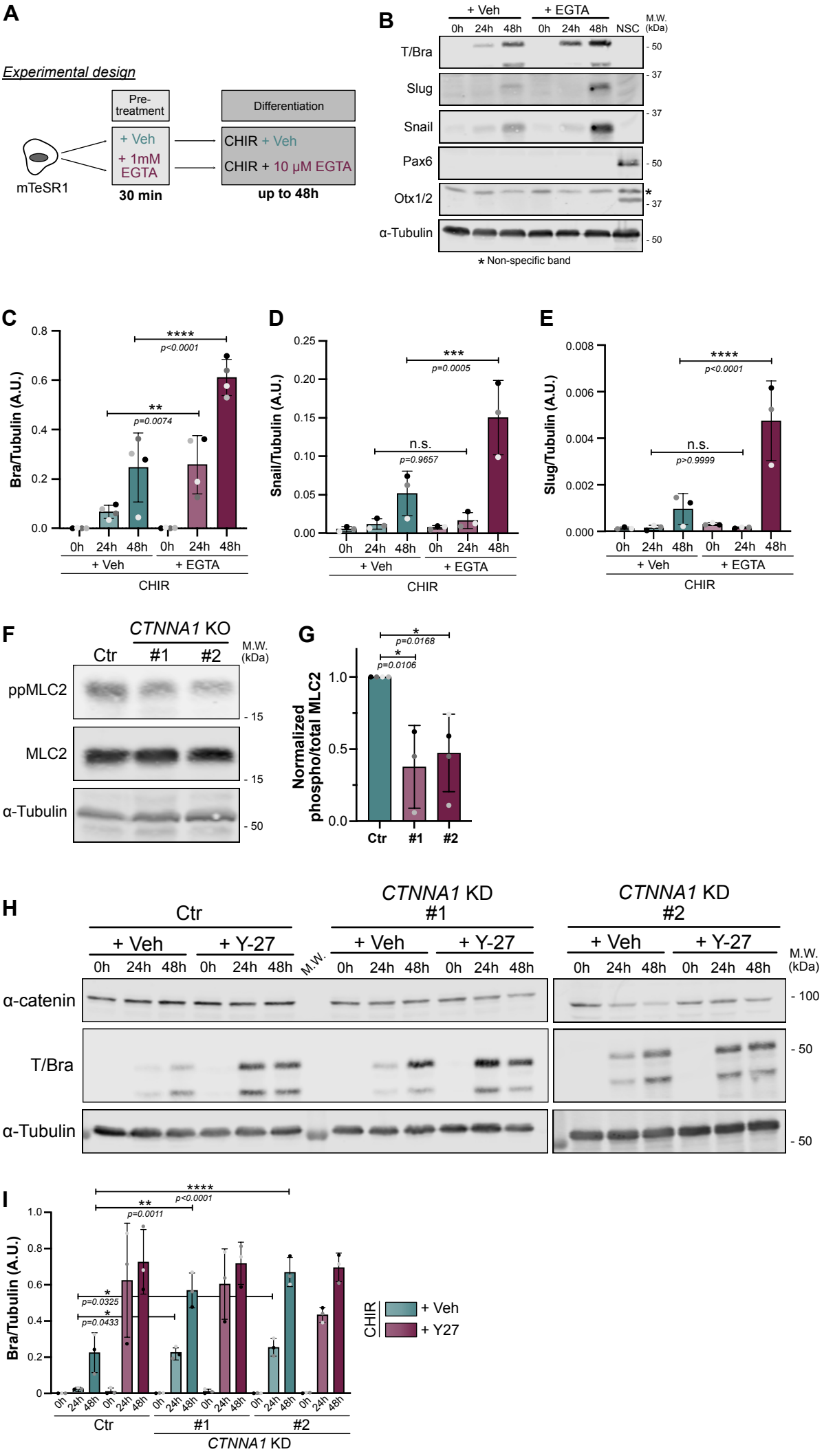
A
Experimental design
Pre-treatment
Differentiation
+ Veh
+ 1mM EGTA
CHIR + Veh
CHIR + 10 µM EGTA
mTeSR1
30 min
up to 48h
B
+ Veh
+ EGTA
0h 24h 48h 0h 24h 48h NSC
M.W. (kDa)
T/Bra
Slug
Snail
Pax6
Otx1/2
α-Tubulin
- 50
- 37
- 37
- 50
- 37
- 50
* Non-specific band
C
Bra/Tubulin (A.U.)
****
p<0.0001
**
p=0.0074
0h 24h 48h 0h 24h 48h
+ Veh
+ EGTA
CHIR
D
Snail/Tubulin (A.U.)
***
p=0.0005
n.s.
p=0.9657
E
Slug/Tubulin (A.U.)
****
p<0.0001
n.s.
p>0.9999
F
CTNNA1 KO
Ctr
#1
#2
M.W. (kDa)
ppMLC2
MLC2
α-Tubulin
- 15
- 15
- 50
G
Normalized phospho/total MLC2
*
p=0.0168
*
p=0.0106
Ctr
#1
#2
H
Ctr
CTNNA1 KD #1
CTNNA1 KD #2
+ Veh
+ Y-27
0h 24h 48h
M.W.
M.W. (kDa)
α-catenin
T/Bra
α-Tubulin
- 100
- 50
- 50
I
Bra/Tubulin (A.U.)
****
p<0.0001
**
p=0.0011
*
p=0.0325
*
p=0.0433
CHIR
+ Veh
+ Y27
Ctr
#1
#2
CTNNA1 KD

Figure 5

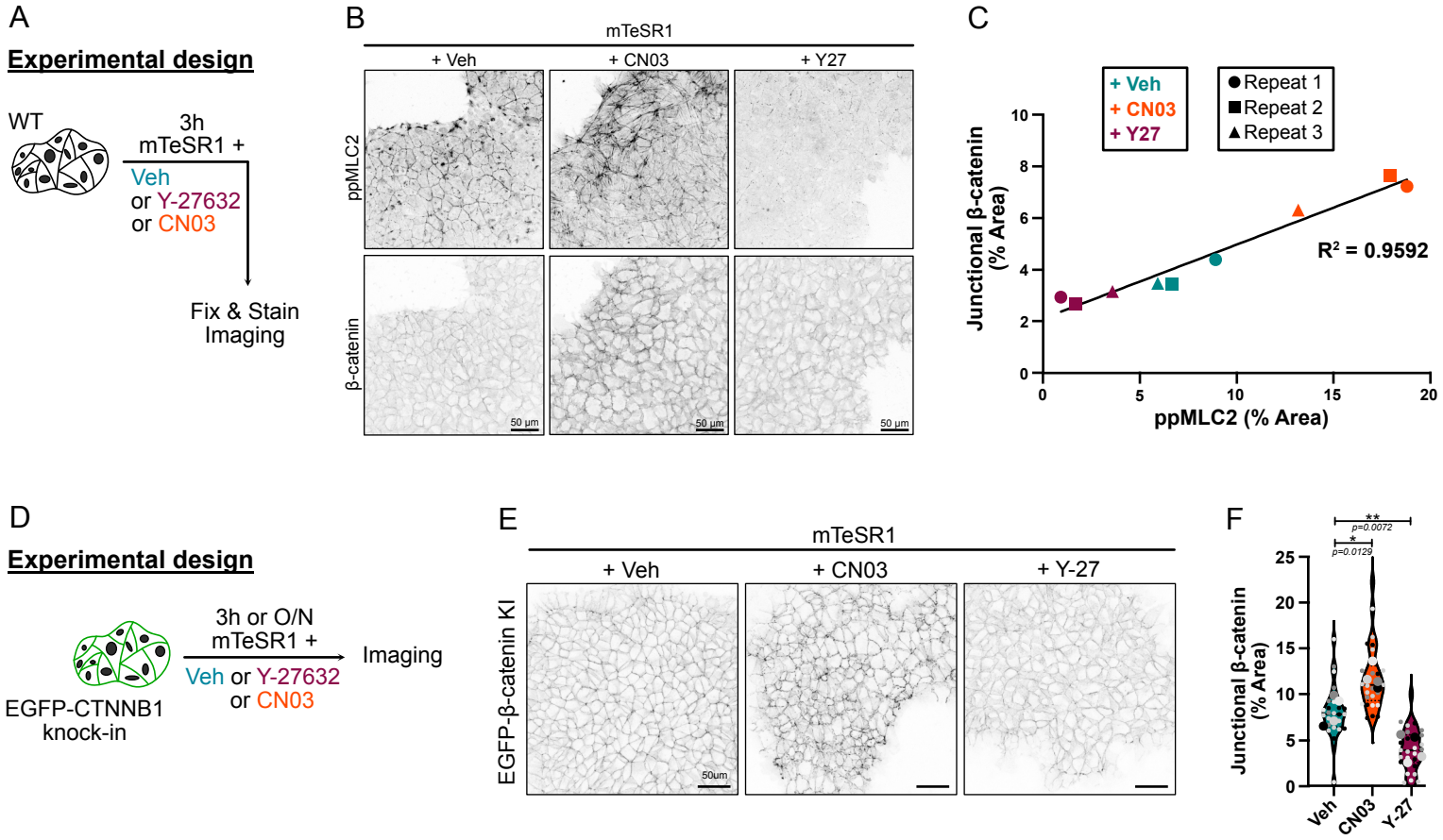
A
Experimental design
WT
3h
mTeSR1 +
Veh
or Y-27632
or CN03
Fix & Stain
Imaging
B
mTeSR1
+ Veh
+ CN03
+ Y27
ppMLC2
β-catenin
50 µm
C
+ Veh
+ CN03
+ Y27
Repeat 1
Repeat 2
Repeat 3
R² = 0.9592
Junctional β-catenin (% Area)
ppMLC2 (% Area)
D
Experimental design
3h or O/N
mTeSR1 +
Veh or Y-27632
or CN03
Imaging
EGFP-CTNNB1
knock-in
E
mTeSR1
+ Veh
+ CN03
+ Y-27
EGFP-β-catenin KI
50um
F
p=0.0072
p=0.0129
Junctional β-catenin (% Area)
Veh
CN03
Y-27

Figure 6

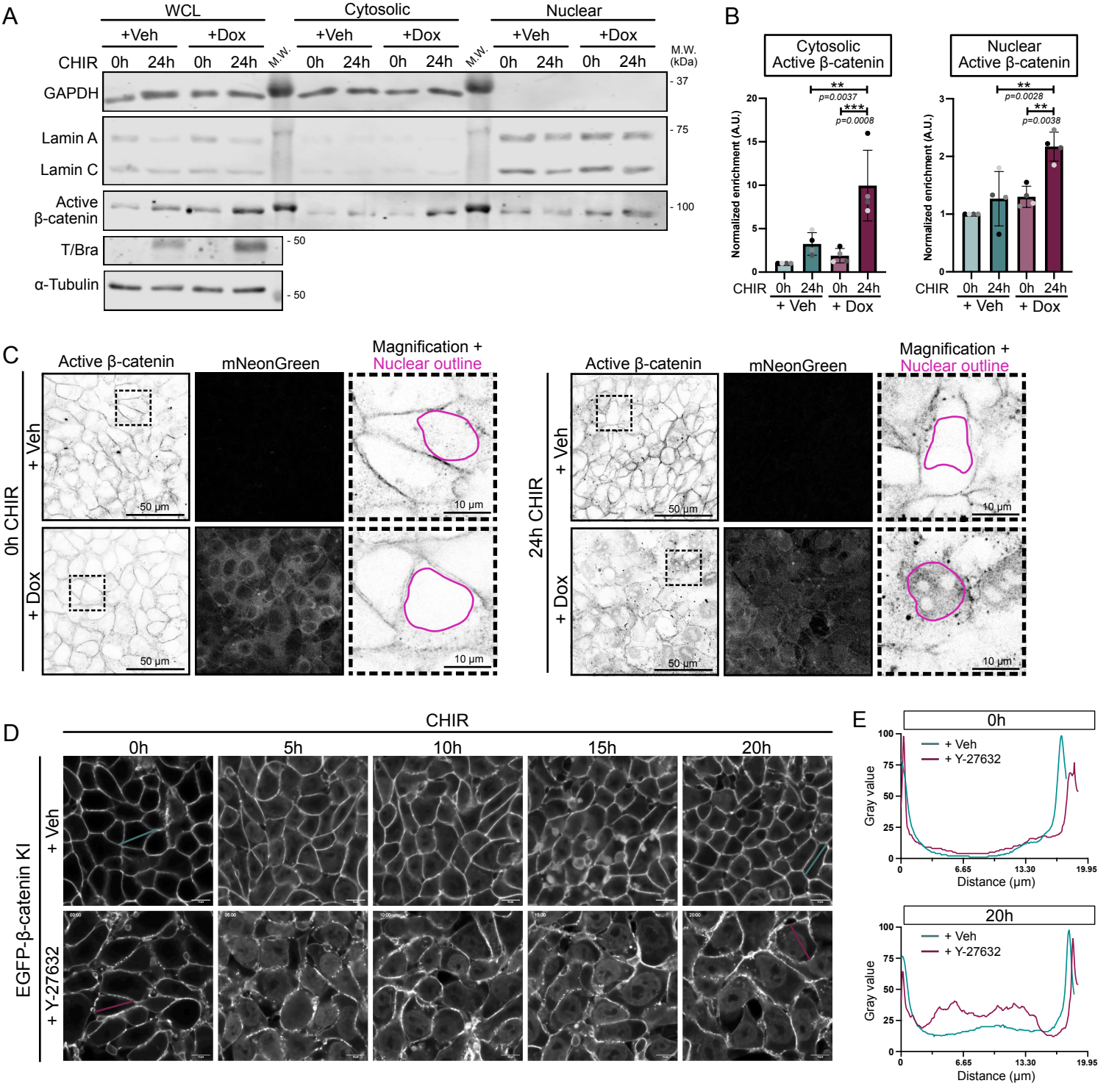
A
WCL
Cytosolic
Nuclear
+Veh
+Dox
CHIR 0h 24h 0h 24h M.W. 0h 24h 0h 24h M.W. 0h 24h 0h 24h
M.W. (kDa)
GAPDH
Lamin A
Lamin C
Active β-catenin
T/Bra
α-Tubulin
- 37
- 75
- 100
- 50
- 50
B
Cytosolic Active β-catenin
Nuclear Active β-catenin
Normalized enrichment (A.U.)
p=0.0037
p=0.0008
p=0.0028
p=0.0038
CHIR 0h 24h 0h 24h
+ Veh + Dox
C
Active β-catenin
mNeonGreen
Magnification + Nuclear outline
0h CHIR
24h CHIR
+ Veh
+ Dox
50 µm
10 µm
D
CHIR
0h
5h
10h
15h
20h
EGFP-β-catenin KI
+ Veh
+ Y-27632
E
0h
20h
+ Veh
+ Y-27632
Gray value
Distance (µm)
F
Experimental design
EGFP-CTNNB1 hiPSCs
+ Veh
+ Y-27
0h or 24h CHIR + Veh
0h or 24h CHIR + Y-27
NE
Lysis
LSB
Insoluble
GFP-Trap
Pull Down
G
Input
Pull Down
Insoluble
0h 24h
Veh Y-27 Veh Y-27
M.W. (kDa)
GFP
TCF4
α-Tubulin
- 100
- 50
- 50
H
Normalized binding (Prey/bait)
n.s.
p=0.6185
p=0.0199
Veh Y-27 Veh Y-27
0h 24h
I
CUT & RUN assay
TBXT
Normalized binding enrichment
n.s.
p=0.3867
p=0.0155
IgG Veh Y-27 Veh Y-27
0h 24h

Figure 7

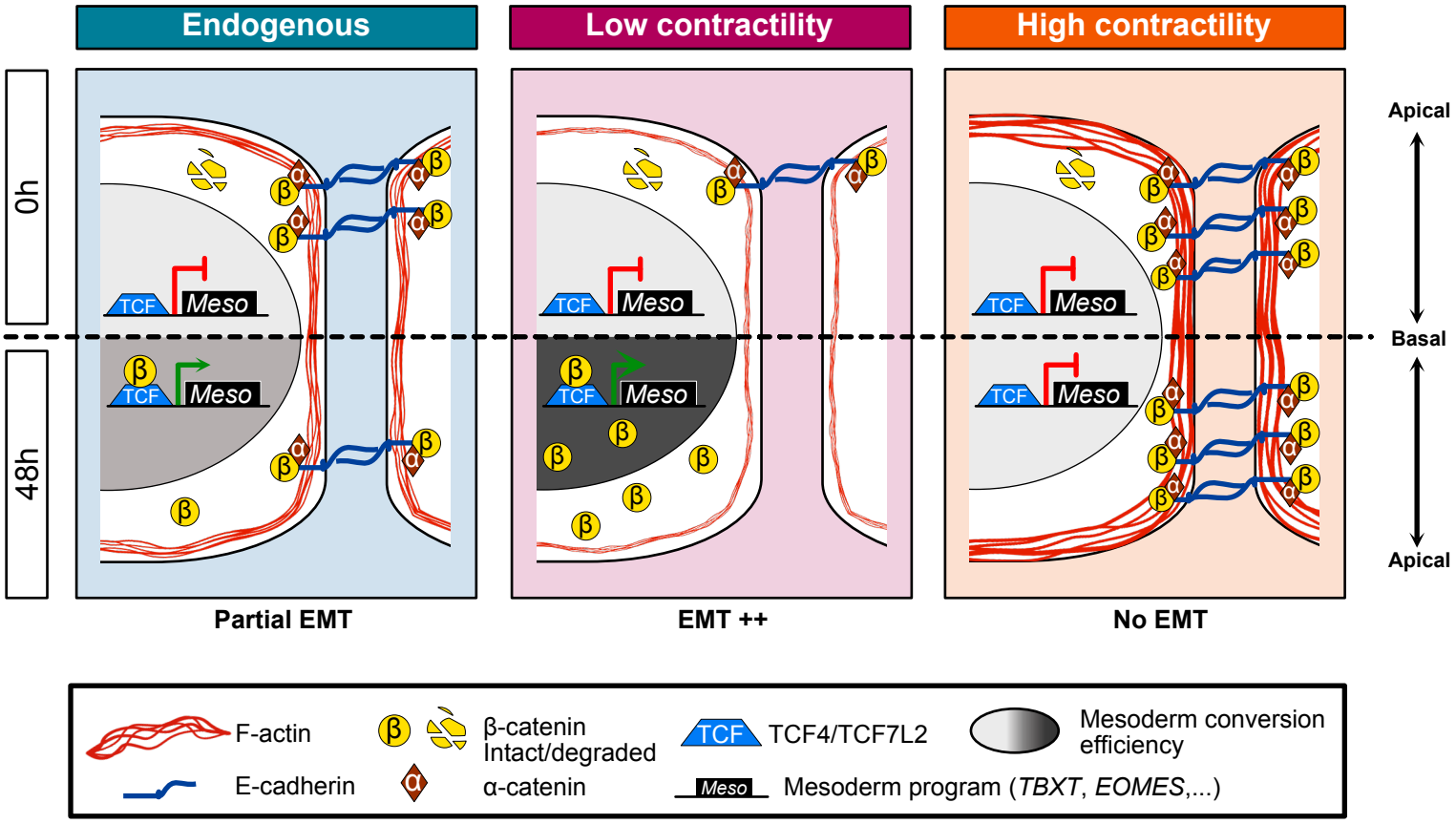
Endogenous
Low contractility
High contractility
0h
48h
Apical
Basal
Apical
TCF
Meso
Partial EMT
EMT ++
No EMT
F-actin
E-cadherin
β-catenin
Intact/degraded
α-catenin
TCF4/TCF7L2
Mesoderm program (TBXT, EOMES,...)
Mesoderm conversion
efficiency

Supplementary Figure 1 - Related to Figure 1

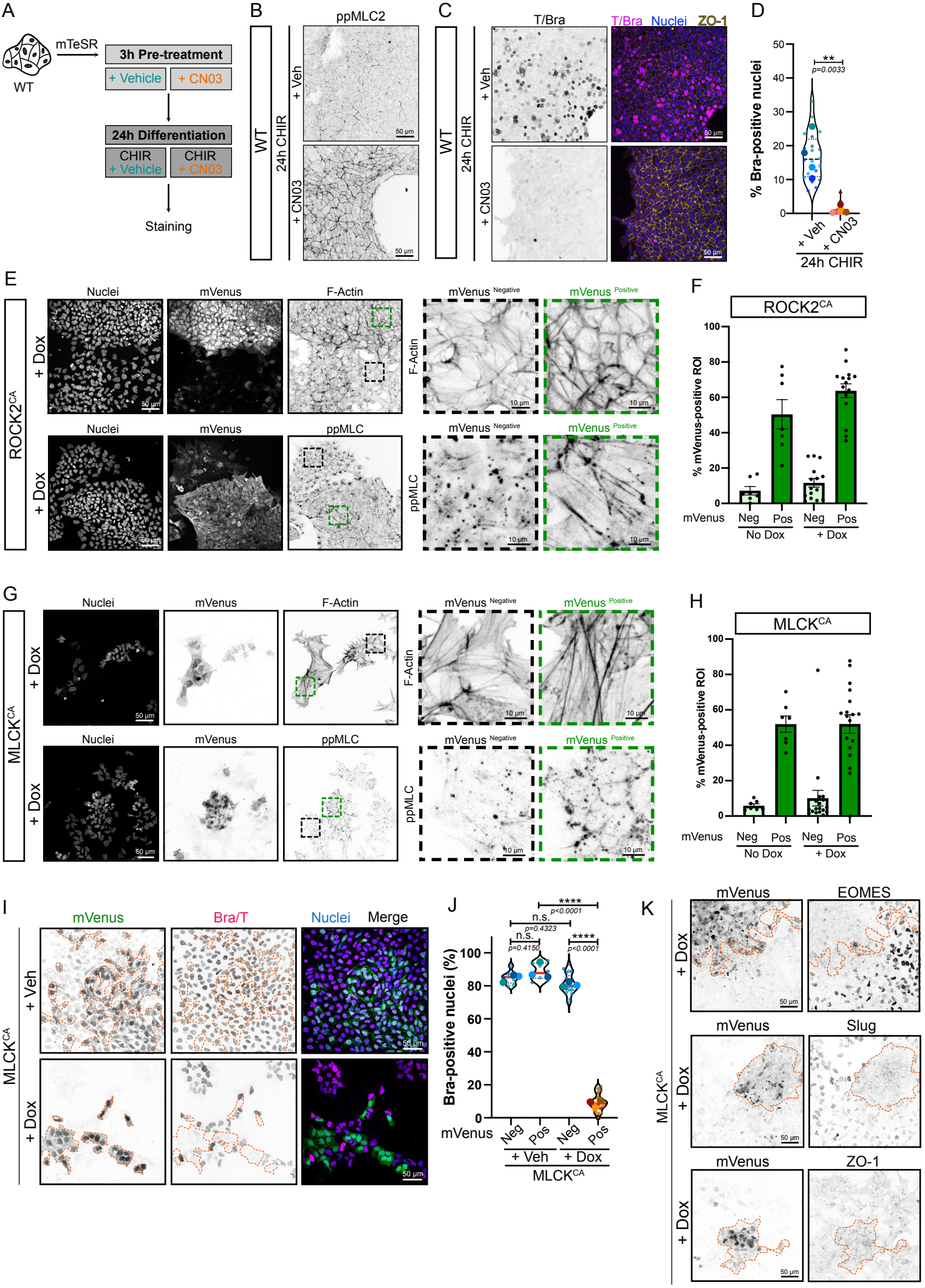

Supplementary Figure 2 - Related to Figure 3

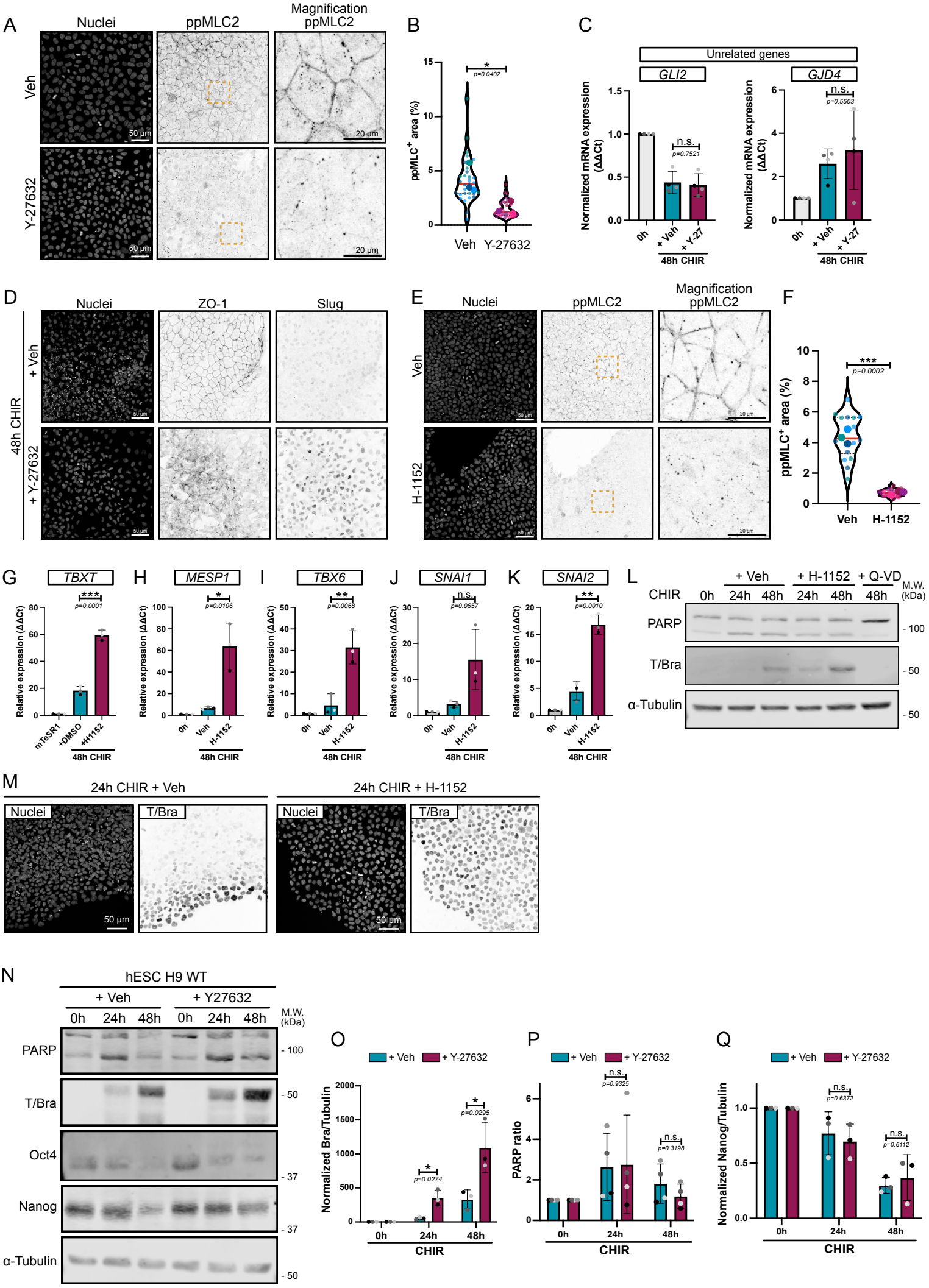

Supplementary Figure 3

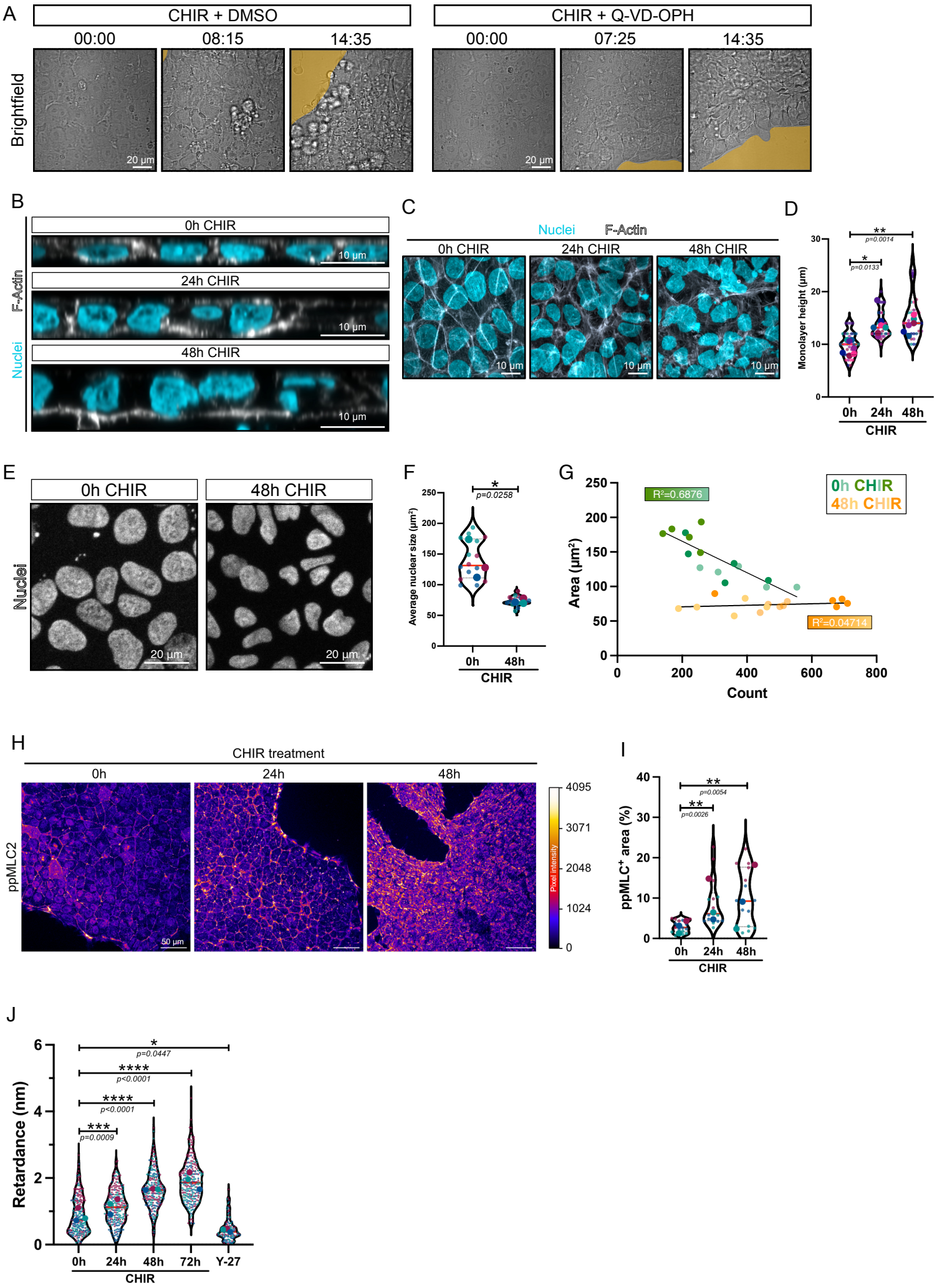

Supplementary Figure 4

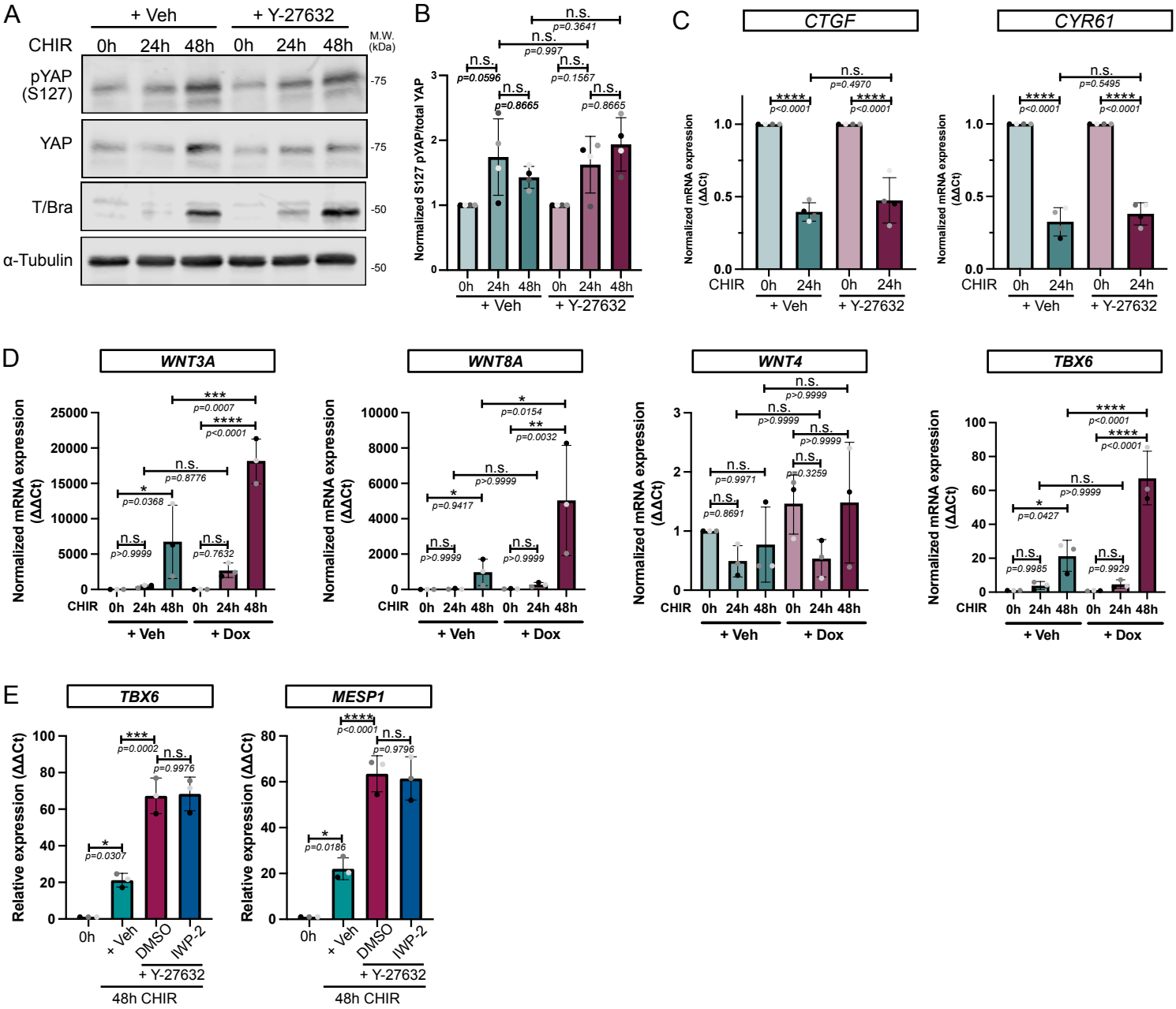

Supplementary Figure 5 - Related to Figure 4

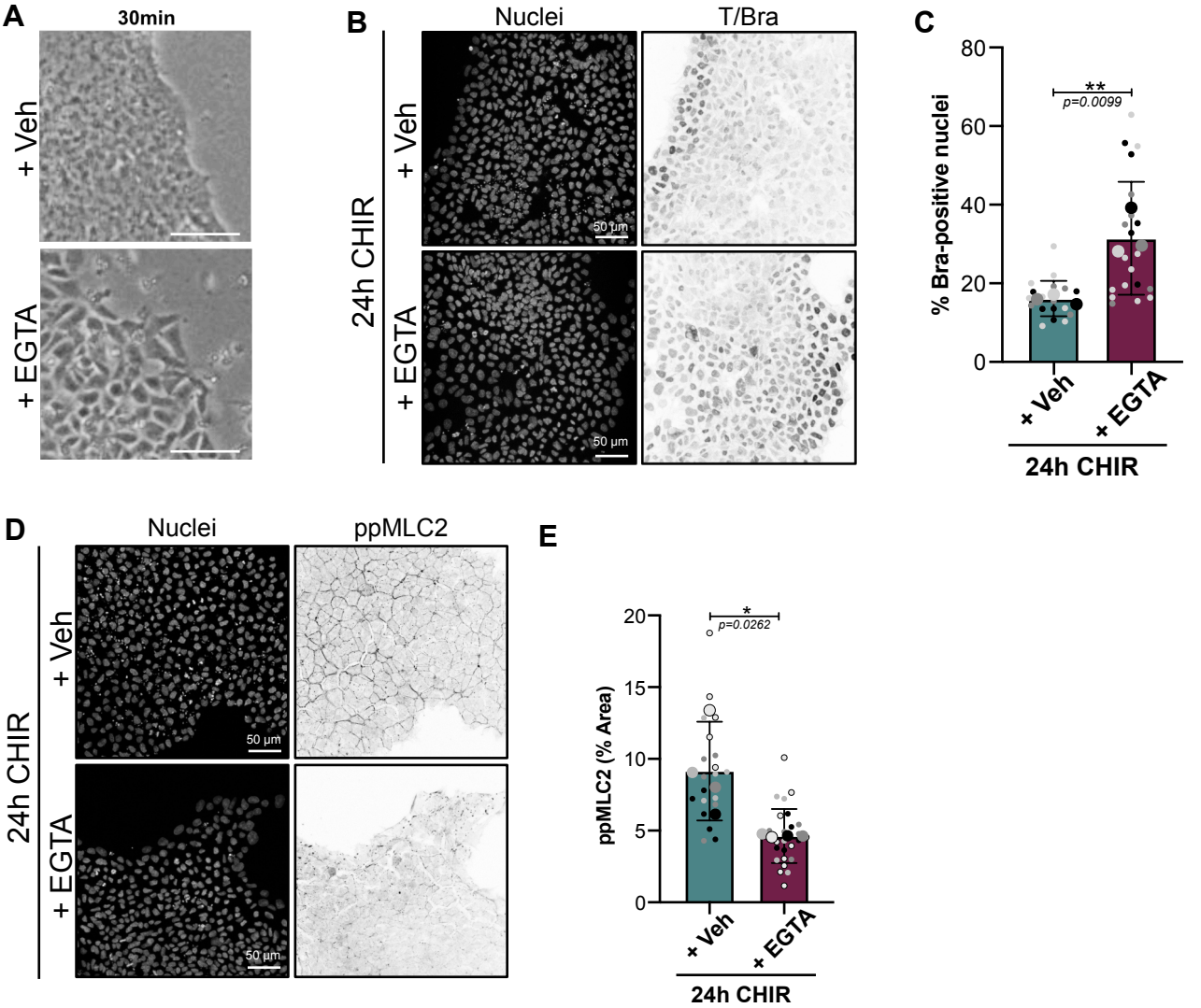

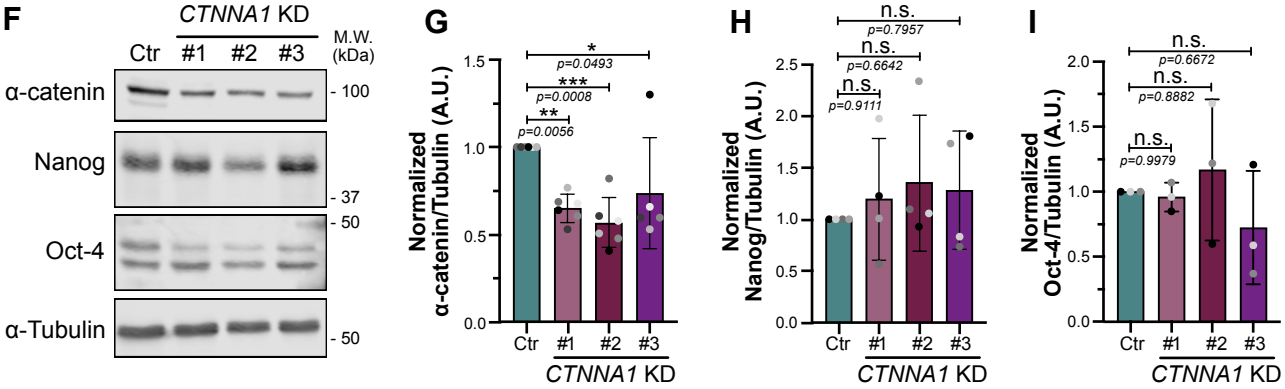

Supplementary Figure 6 - Related to Figure 5

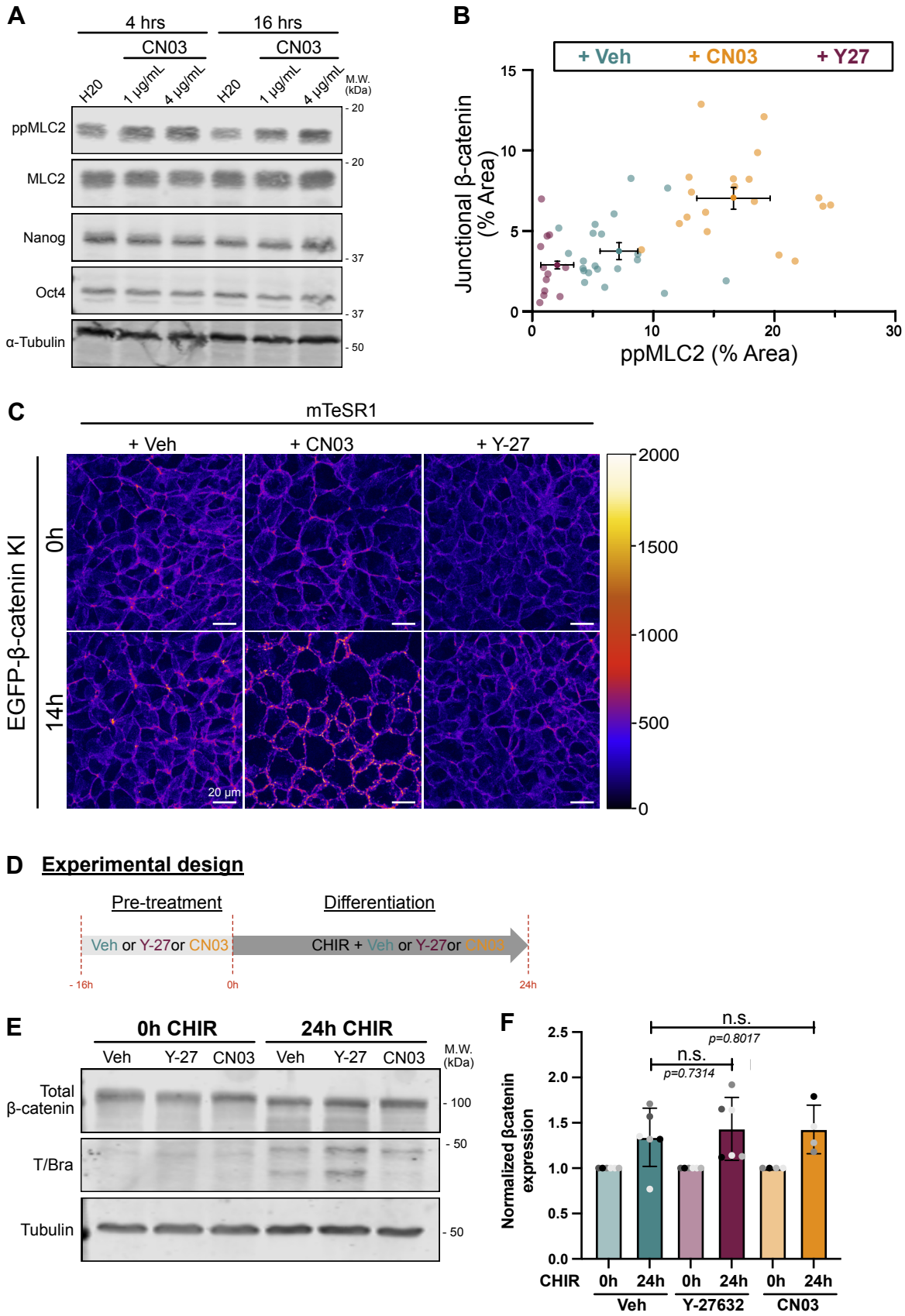
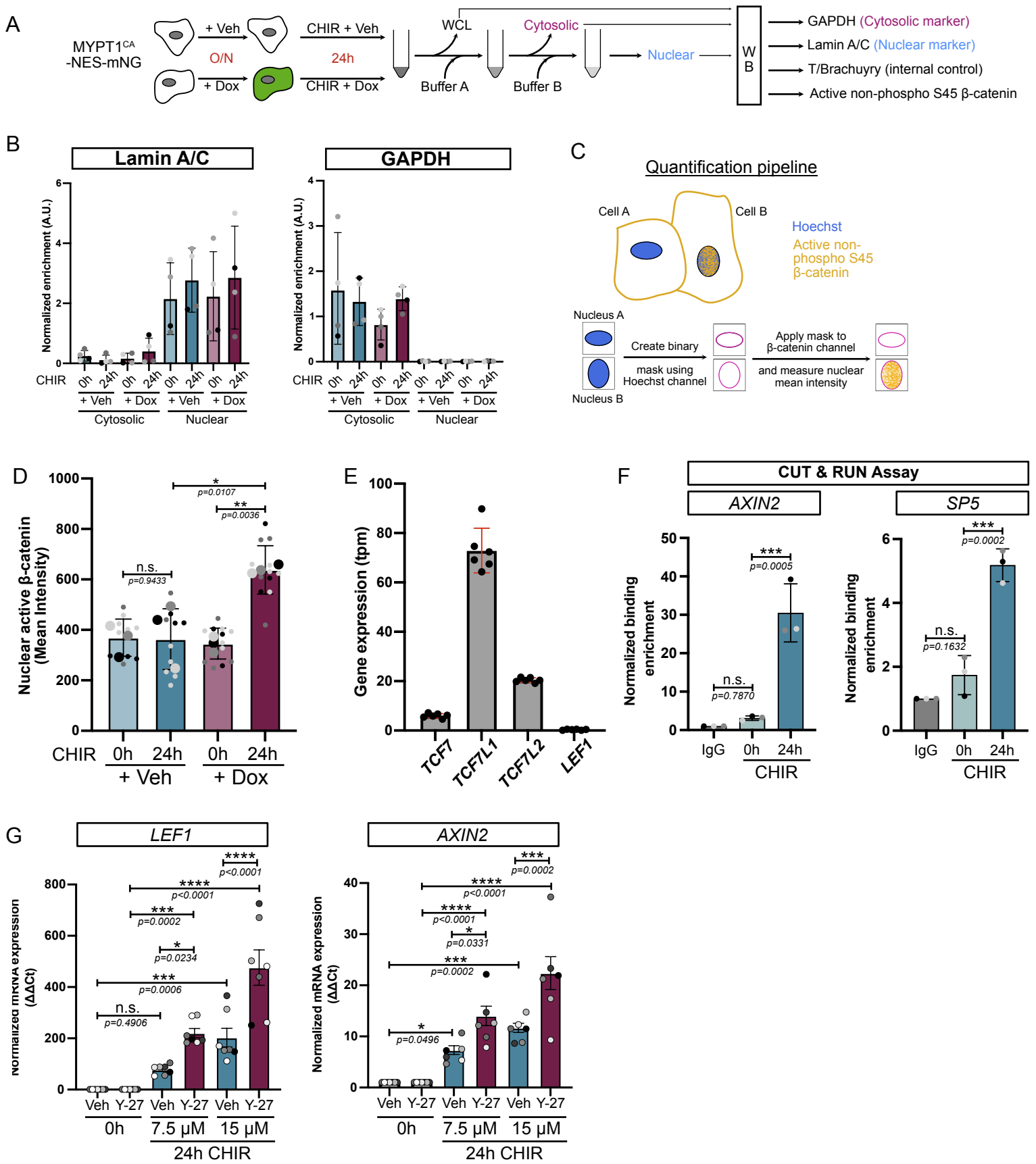
Supplementary Figure 7 - Related to Figure 6